

Article

Dynamic Mode Decomposition of Fluorescence Loss in Photobleaching Microscopy Data for Model-Free Analysis of Protein Transport and Aggregation in Living Cells

Daniel Wüstner 

Department of Biochemistry and Molecular Biology and Physics of Life Sciences (PhyLife) Center, University of Southern Denmark, Campusvej 55, DK-5230 Odense, Denmark; wuestner@bmb.sdu.dk

Abstract: The phase separation and aggregation of proteins are hallmarks of many neurodegenerative diseases. These processes can be studied in living cells using fluorescent protein constructs and quantitative live-cell imaging techniques, such as fluorescence recovery after photobleaching (FRAP) or the related fluorescence loss in photobleaching (FLIP). While the acquisition of FLIP images is straightforward on most commercial confocal microscope systems, the analysis and computational modeling of such data is challenging. Here, a novel model-free method is presented, which resolves complex spatiotemporal fluorescence-loss kinetics based on dynamic-mode decomposition (DMD) of FLIP live-cell image sequences. It is shown that the DMD of synthetic and experimental FLIP image series (DMD-FLIP) allows for the unequivocal discrimination of subcellular compartments, such as nuclei, cytoplasm, and protein condensates based on their differing transport and therefore fluorescence loss kinetics. By decomposing fluorescence-loss kinetics into distinct dynamic modes, DMD-FLIP will enable researchers to study protein dynamics at each time scale individually. Furthermore, it is shown that DMD-FLIP is very efficient in denoising confocal time series data. Thus, DMD-FLIP is an easy-to-use method for the model-free detection of barriers to protein diffusion, of phase-separated protein assemblies, and of insoluble protein aggregates. It should, therefore, find wide application in the analysis of protein transport and aggregation, in particular in relation to neurodegenerative diseases and the formation of protein condensates in living cells.

Keywords: photobleaching; time-lapse microscopy; model reduction; biomolecular condensates; protein aggregation; intracellular transport



Citation: Wüstner, D. Dynamic Mode Decomposition of Fluorescence Loss in Photobleaching Microscopy Data for Model-Free Analysis of Protein Transport and Aggregation in Living Cells. *Sensors* **2022**, *22*, 4731. <https://doi.org/10.3390/s22134731>

Academic Editors: Huangxian Ju and Nicole Jaffrezic-Renault

Received: 7 April 2022

Accepted: 20 June 2022

Published: 23 June 2022

Publisher's Note: MDPI stays neutral with regard to jurisdictional claims in published maps and institutional affiliations.



Copyright: © 2022 by the author. Licensee MDPI, Basel, Switzerland. This article is an open access article distributed under the terms and conditions of the Creative Commons Attribution (CC BY) license (<https://creativecommons.org/licenses/by/4.0/>).

1. Introduction

Fluorescence microscopy has enormous potential in determining the dynamics and interactions of proteins in living cells. In particular, genetically encoded fluorescent protein tags, such as green fluorescent protein and its color variants, combined with powerful live-cell imaging, have revolutionized our understanding of protein dynamics and compartmentalization. The analysis of such complex imaging data is challenging, and a variety of quantitative image analysis techniques have been developed for interrogating the intracellular transport of proteins and other biomolecules. One group of such techniques comprised of fluorescence recovery after photobleaching (FRAP), fluorescence loss in photobleaching (FLIP), and continuous photobleaching (CP), employ the photobleaching of a small fraction of the tagged protein population using short laser pulses to perturb the steady-state fluorescence distribution [1–3]. Here, the analysis is based on determining the response of the system to the perturbation. The same principle underlies the analysis of photoactivation microscopy data [4,5]. FRAP and FLIP are easy to implement in a cell biological laboratory, requiring only conventional fluorescent protein constructs, often providing fast qualitative insight into protein dynamics. Determining the diffusion and binding constants as well as the exchange parameters between compartments from FRAP or FLIP data is also possible, but this requires elaborate computational approaches to

solve and parametrize the underlying partial differential equation systems [6,7]. Often, parameter estimation is based on various assumptions, which are highly context-dependent and therefore difficult to transfer between different laboratories and setups. For selected biological systems, such as transcription-factor binding to DNA, cross-validation has shown that parameter estimates for diffusion and binding can be compared for three approaches, i.e., fluctuation, photobleaching, and single-molecule microscopy [8–10].

FLIP microscopy is based on the repeated photobleaching of a small cellular region and observing the fluorescence loss kinetics, caused by transport to the bleached area, throughout the entire cell. FLIP, therefore, has an advantage over FRAP; it provides not only full spatiotemporal protein dynamics, but also the sampled time scale that can be tuned by adjusting the pause time between laser pulses. Fast, repeated bleaching can result in diffusion-limited fluorescence loss with pronounced fluorescence gradients of the tagged protein, as protein diffusion is too slow to replenish bleached molecules immediately [11]. Slow bleaching, i.e., longer pauses between the laser pulses allows for diffusion to keep up with bleaching, such that diffusion is no longer limiting fluorescence-loss kinetics (bleach-limited FLIP). In this case, fluorescence-loss kinetics report primarily on barriers to diffusion, such as transport across the nuclear membrane and binding and the release of a protein to a subcellular structure or on diffusion barriers, such as that between the soma and axon in neurons [11,12]. Thus, FLIP has the potential to reveal barriers to diffusion in addition to the determination of diffusion and binding constants. In this regard, FLIP microscopy can be compared with pair correlation analysis of protein diffusion and confinement [11,13–17]. FLIP is also extensively used to study biomolecular condensates, which contribute to cellular compartmentalization by forming membrane-less organelles via liquid–liquid phase separation [18].

Protein aggregation is a hallmark of a number of neurodegenerative diseases, including Alzheimer's (aggregation of Tau and Amyloid-beta protein), amyotrophic lateral sclerosis (TDP-43 protein), frontotemporal lobar degeneration (FUS protein), Parkinson's disease (Alpha-synuclein aggregation), and Huntington's disease (aggregation of mutant Huntingtin protein) [19]. In Huntington's diseases and various forms of Ataxia, an extended polyglutamine stretch in disease variants of the affected protein causes a higher tendency for self-interaction via these disordered protein regions, leading to the formation of protein condensates/aggregates, sometimes called inclusion bodies [20–23]. For many of the above-mentioned proteins, it has been shown that the formation of stable intracellular aggregates is preceded by the formation of soluble protein condensates, which can still exchange molecules with the surrounding cytoplasm on a time scale of minutes or less, as shown in FRAP and FLIP experiments [20–26]. They are also often rounded in shape in contrast to stable aggregates, which form fibrils and are of irregular shape, suggesting that, in liquid protein condensates, surface tension is a determining factor in their stability [19,23,26]. Over time, protein molecules in these droplet-like aggregates strengthen their interactions, leading to a gel-like state and, eventually, to amyloid-like fibrils, as observed in brain dissections of affected patients [19,27]. The different physico-chemical properties of soluble protein condensates versus stable fibrils are reflected in their dynamics, and, for several neurotoxic proteins, fast and slowly exchanging populations have been detected [25,28,29]. The aggregation process can be sped up by extending the polyglutamine stretch and reduced by the presence of chaperonins. For example, extending the polyglutamine tract in mutant Huntingtin (mtHtt) causes a transition from soluble liquid-like protein condensates to solid-like fibrils, as studies by FRAP, fluorescence lifetime and anisotropy imaging, single molecule tracking, and fluorescence fluctuation techniques [20,29–38]. We have previously used computational FLIP to characterize the dynamic properties of mtHtt with 73 repetitions of glutamine tagged with enhanced green fluorescent protein (eGFP-Q73). A residence time for this protein of 16–83 sec in cytoplasmic inclusion bodies was found [11,39]. Using a reaction–diffusion model, we also determined diffusion constants and rate constants for nucleo-cytoplasmic exchange of this protein, and we found that it can diffuse about 30 μm upon release from a protein condensate before being recaptured and incorporated into

another aggregate [39,40]. Diffusion, rather than active transport, has been suggested to drive the aggregation of polyglutamine proteins in living cells [31].

Data-driven machine learning methods are increasingly used to analyze complex spatiotemporal processes. Dynamic mode decomposition (DMD) is a novel, data-driven approach to extract dynamic information from large spatiotemporal datasets, such as images. Increasingly, it is being applied in computer vision and biomedical imaging [41,42]. DMD has been used to detect video shots or discriminate foreground from background in videos of natural scenes; it has also been used to segment images of human kidneys and detect functional brain states by magnetic resonance imaging image sequences [43–46]. In a recent study, the potential of DMD for use in the analysis of microscopy data was demonstrated by determining the photobleaching characteristics of fluorescent probes to distinguish probe fluorescence from cellular autofluorescence [47]. Here, DMD is applied to analyze simulated FLIP images and FLIP sequences of enhanced green fluorescent protein (eGFP) and of eGFP-tagged mtHtt (eGFP-mtHtt). DMD is demonstrated to be a powerful tool to decompose the intracellular dynamics of these proteins in distinct subcellular compartments, effectively detecting barriers to intracellular protein diffusion. Using DMD, the dynamics of eGFP-mtHtt in rapidly and slowly exchanging protein aggregates is analyzed. DMD-FLIP is shown not only to allow for the kinetic identification of phase-separated proteins and stable protein aggregates, but also for the efficient spatial and temporal denoising of FLIP image sequences.

2. Materials and Methods

2.1. Cell Culture and Transfection

McArdle RH7777 (McA) cells expressing the enhanced green fluorescent protein (eGFP) were reported and used for FLIP experiments, as described previously [11]. They were grown in DMEM with 4.5 g/L glucose, supplemented with 10% heat-inactivated FCS and antibiotics. Chinese hamster ovarian (CHO) cells were purchased from ATCC (www.atcc.org; LGC Standards Office Europe, AB, Borås, Sweden) and grown in bicarbonate-buffered Ham's F-12 medium supplemented with 5% fetal calf serum (FCS) and antibiotics. McA and CHO cells were routinely passaged in plastic tissue culture dishes. CHO cells were transiently transfected with mHtt bearing the N-terminus of Huntingtin and an extended polyglutamine stretch of 145 residues and a C-terminal eGFP-tag, using lipofectamine, following the manufacturer's instructions (SIGMA-Aldrich, Søborg, Denmark). All cells were seeded on microscope slide dishes coated with poly-D-lysine, 2–3 days prior to experiments and kept in buffer medium containing 150 mM NaCl, 5 mM KCl, 1 mM CaCl₂, 1 mM MgCl₂, 5 mM glucose, and 20 mM HEPES (pH 7.4) for imaging.

2.2. Image Simulation

To validate the procedure, synthetic FLIP image sequences were generated using the Macro language of ImageJ (<https://imagej.nih.gov/ij/> accessed on 6 February 2021), as described previously [11]. This included a three-compartment model for the protein exchange between nucleus, N , and cytoplasm, C , with rate constants, k_1 and k_{-1} ; the release of protein from cytoplasmic aggregates, A , with rate constant, k_2 ; as well as photobleaching in a localized region of the cytoplasm with rate constant, k_3 . Assuming a well-mixed system (i.e., bleach-limited FLIP, see Introduction), diffusion can be ignored, and one obtains the analytical solutions given in Appendix A.

2.3. FLIP Microscopy of Fluorescent Proteins in Living Mammalian Cells

In FLIP microscopy, a strong and short laser pulse is used to photobleach a suitably tagged biomolecule (e.g., a labeled protein, lipid, or RNA molecule) locally, and the fluorescence loss of the tagged molecule in other cellular regions is monitored (Figure 1A). If the labeled molecular species, for example, eGFP-mtHtt, can exchange between its initial position and the bleached region, the fluorescence loss will be observed in the area of its initial localization. If the protein is confined to a region, e.g., to subcellular aggregates, no

fluorescence loss will be observed in those aggregates (green circular regions in Figure 1A). If some protein exchange can take place, for example between the cytoplasm and the phase-separated, but liquid-like, protein condensates (green ellipsoidal regions in Figure 1A), it will be delayed compared to the free cytosolic protein pool. Thus, the fluorescence-loss kinetics report about the exchange dynamics of a tagged protein translocating between subcellular compartments. FLIP microscopy was performed using a confocal laser-scanning fluorescence microscope (Zeiss LSM 510 META, Zeiss, Jena, Germany) equipped with a 63x 1.4 NA plan Apochromat water-immersion objective with temperature control at 37 °C (Zeiss, Jena, Germany). The fluorescence of eGFP was collected with a 505–530 bandpass filter after excitation with a 25-milliwatt argon laser emitting at 488 nm. FLIP experiments were performed by first defining regions of interest which were repeatedly bleached, while an image was acquired with reduced laser power (0.5% output) at the start of the experiment and after each bleaching event. A pause between the bleaching events ensured some recovery in the bleached region. Images were acquired using the time-lapse function of the Zeiss LSM510 Meta confocal system. The microscope was located at a nitrogen-floated table to prevent vibrations and focus drift and contained a temperature-controlled stage maintained at 35 ± 1 °C.

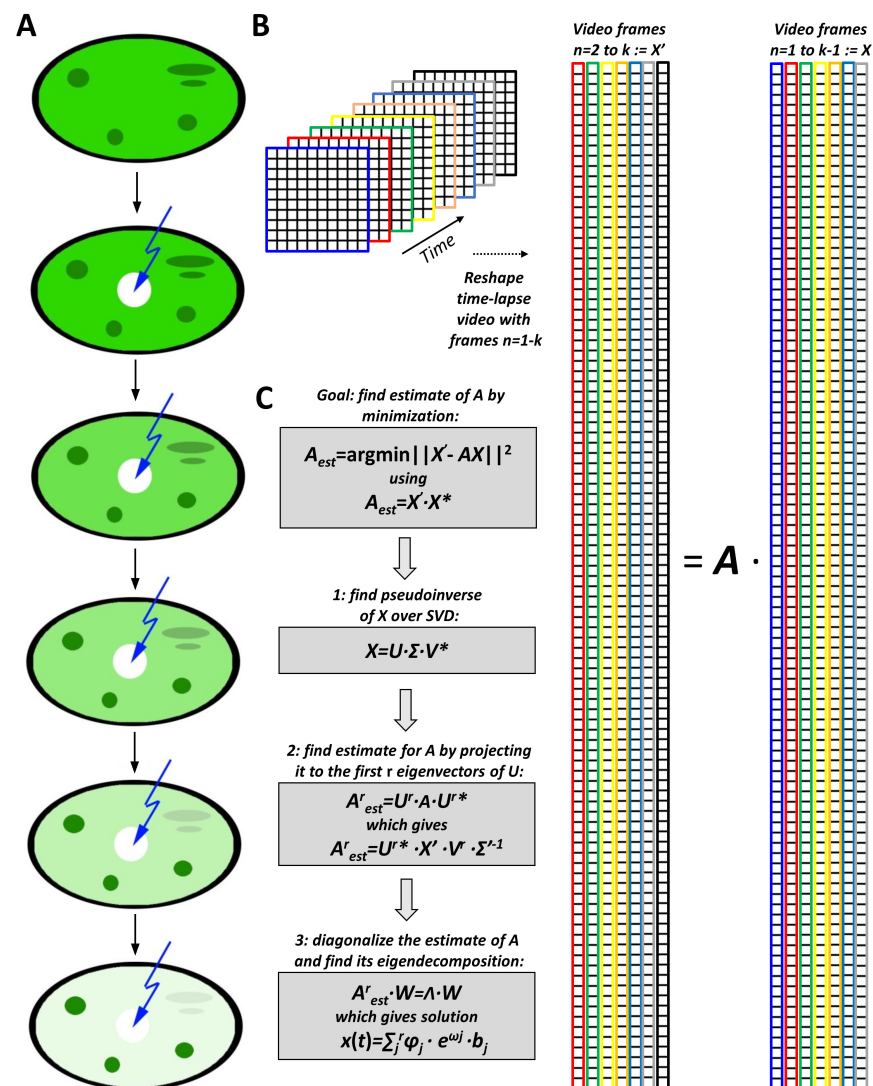


Figure 1. Principle of DMD-FLIP microscopy. Fluorescence loss in photobleaching (FLIP) is based on the repeated bleaching of a small subcellular area and monitoring fluorescence loss in the entire cell

by intervening confocal image acquisition (**A**). For subsequent DMD analysis, the FLIP time-lapse image sequence is reshaped into two matrices, in which each image becomes a column (**B**). The first matrix, X , runs from the first image ($n = 1$, blue) to the next last image ($n = k - 1$, grey) stacked as columns. The second matrix, X' , runs from the second image ($n = 2$, red) to the last image of the video ($n = k$, black). The time-evolution of the video sequence is modeled as a matrix equation of the form $X' = A \cdot X$, and the aim of DMD is to find the best possible approximation to this matrix (**C**). A singular-value decomposition of X allows for a rank- r approximation with the most dominant singular values giving the rank-reduced matrix, X^r . The pseudoinverse of this matrix can be computed, which allows for deriving an estimate of the matrix A , which is A^r_{est} . Spectral decomposition of this matrix provides its eigenvectors as columns of the matrix, W , and corresponding eigenvalues organized in the matrix, Λ . A linear combination of the derived dynamic modes, φ_j , mode amplitudes, b_j , and eigenvalues, $\omega_j = \log(\lambda_j)/\Delta t$, allows for reconstructing the full dynamic information of the original image data. Note that $'^*$ indicates the conjugate transpose of a matrix.

2.4. Outline of the DMD Method Applied to Fluorescence Microscopy Data

The first step in applying DMD to FLIP microscopy data is that the FLIP image stack, $I(x, y, t)$, of the fluorescence intensity, I , as a function of spatial coordinates, x, y and time, t , is reshaped into $u \cdot v \cdot 1$ column vectors, \bar{x}_n , called snapshots in the DMD literature, which become arranged in a j times k data matrix, X (Figure 1B). This matrix consists of i rows, which are the pixels of each image reshaped into a vector, and k columns, each representing one time point of the original image sequence [41,45]:

$$X = [\bar{x}_1, \bar{x}_2, \dots, \bar{x}_n, \dots, \bar{x}_{k-1}] \quad (1)$$

Here, the index $n = 1, \dots, k - 1$ indicates the frame number that is equivalent to the time axis of the video image sequence. Separately, a second matrix is formed from the video sequence in which the second to k th frame is reshaped as described above giving (Figure 1B, most right matrix):

$$X' = [\bar{x}_2, \dots, \bar{x}_n, \dots, \bar{x}_k] \quad (2)$$

DMD aims to find the optimal mapping between discrete time steps, Δt , represented by these matrices, which describes the advancement of the system in the time described by the matrix A , which approximates the Koopman operator [42]:

$$X' = A \cdot X \quad (3)$$

This can be achieved as outlined in Figure 1C, by minimizing the Frobenius norm, $\|\cdot\|_F$ [42]:

$$A := \operatorname{argmin} \|X' - A \cdot X\|_F = X' \cdot X^* \quad (4)$$

One can find the pseudoinverse of the first data matrix, X^* , by using a singular value decomposition (SVD) of X into unitary matrices U and V^* with singular values in the diagonal matrix Σ :

$$X = U \cdot \Sigma \cdot V^* \quad (5)$$

The original matrices X and X' are of size $i \times k$, with many more rows (i.e., pixels, typically 512×512 , resulting in 262,144 rows, i) than time points (i.e., columns, k). Thus, A is a 'tall-skinny' matrix, since image dimension is larger than number of snapshots in time (Figure 1B). Accordingly, A has at most, k nonzero singular values and corresponding singular vectors and is maximally of rank k [42]. One can therefore approximate A by calculating its projection onto the leading singular vectors, which gives a much smaller matrix A' of maximal size $k \times k$. We obtain [42,43]:

$$A' = U'^* \cdot A \cdot U' = U'^* \cdot X_2 \cdot V' \cdot \Sigma'^{-1} \quad (6)$$

Often fewer, i.e., only r singular values are needed to describe the signal in the data matrix A (i.e., $r \ll k$), and one can employ a thresholding method to discard all singular values larger than r . Accordingly, the signal content of the full matrix is retained, while the noise is efficiently removed [48,49]. The optimal threshold for the truncation of singular values can be found automatically using the method of Gavish and Donoho [49]. Subsequently, a spectral decomposition of A' provides the DMD modes as eigenfunctions φ_j , (i.e., eigenvectors of A , also called DMD modes), corresponding eigenvalues, λ_j (so-called DMD eigenvalues), and mode amplitudes b_j according to:

$$x_r = \sum_{j=1}^r \varphi_j \cdot \lambda_j^{k-1} \cdot b_j \quad (7)$$

The eigenvalues determined for a rank- r decomposition of the system matrix A , λ_j , for $j = 1, \dots, r$, are logarithmically scaled and divided by the interval time (i.e., the acquisition time in the case of bleach stacks, Δt):

$$\omega_j = \log(\lambda_j) / \Delta t \quad (8)$$

For a continuous-time system using Equation (8), this becomes:

$$x(t) = \sum_{j=1}^r \varphi_j \cdot e^{\omega_j \cdot t} \cdot b_j \quad (9)$$

Thus, the entire FLIP image series is approximated as the sum of eigenfunctions, their weights, and respective eigenvalues (Figure 1). DMD and its accompanying analysis were carried out in Python using Jupyter notebooks (<https://jupyter.org/> accessed on 4 August 2020) and PyDMD, a python library for DMD calculations [50]. FLIP simulations were implemented as Macros in ImageJ (ImageJ (nih.gov)), as described previously [11]. To account for the diffusion of aggregates, a Monte Carlo simulation was used, in which two random numbers were generated from a uniform distribution and transformed to a Gaussian distribution using the Box–Muller method in an ImageJ macro [51]. For a constant diffusion coefficient and fixed time step, a Gaussian step-length distribution is known to exactly simulate normal diffusion [52]. For a simulated pixel size of 0.125 μm and one frame per second, this corresponds to the slow diffusion of the aggregates with a diffusion constant of $D = 0.004 \mu\text{m}^2/\text{s}$, which is comparable to experimental findings for diffusion of small eGFP-mtHtt aggregates in cells [11]. In simulations with flow, a constant value of five percent of a pixel was subtracted in the negative x-direction, corresponding to a flow speed of $v = 0.00625 \mu\text{m}$. All calculations were run on either a zBook laptop computer from HP with Intel i7-8850H 2.6 GHz CPU with 32 GB RAM and an M1000M NVIDIA graphics card (NVIDIA Santa Clara, CA, USA) or on a Desktop workstation with Intel i9 11900 8-core CPU with max. 5.2 GHz and a GeForce RTX 3090 graphics card from NVIDIA (NVIDIA Santa Clara, CA, USA).

3. Results

3.1. DMD of Simulated FLIP Image Sequences

The ability of DMD to decompose FLIP dynamics was first assessed on synthetic image sequences, in which bleaching was assigned to the cytoplasm and the bi-directional exchange between the cytoplasm and the nucleus was explicitly considered. The FLIP simulation also includes protein aggregates in the cytoplasm, from which the protein can be slowly released, whereby its dynamics are coupled to the fluorescence loss in the cytoplasm and nucleus (Figure 2A,B). Simulating this model requires solving a coupled system of ordinary differential equations (ODEs), as described in Appendix A. To simplify the model, protein aggregates are assumed to have already been formed at the beginning of the simulation, without explicitly considering their assembly from protein in the cytoplasm. That means that only a slow protein release from already formed aggregates is considered,

with no rebinding of released protein to the aggregates (Figure 2A). This considerably simplifies the model compared to the reversible exchange between inclusion bodies and cytoplasm and is justified by the high probability of the released protein being bleached by the FLIP laser in the cytoplasm, before eventually rebinding to an aggregate [11]. By calculating the DMD of the data using the optimal-rank option in PyDMD [50], three modes were recovered, the dynamics of which are shown in Figure 2A. Mode 0 had an eigenvalue of close to 1 with slowly changing dynamics ($\lambda_0 = 0.996$, Figure 2B; yellow line and Figure 2C). After rescaling to real time using Equation (8), this corresponds to an eigenvalue of $\omega_0 = -0.00375$, which closely resembles the value used for the negative of the rate constant of fluorescence loss from aggregates in the simulation (i.e., the first eigenvalue of the analytical model, see Equation (A7), $l_1 = -k_2 = -0.005 \text{ s}^{-1}$). Accordingly, this mode describes the fluorescence-loss dynamics in the aggregates and is further supported by the 2D map of mode 0 (Figure 2D). This dynamic mode has the greatest number of negative values at the site of the aggregates, and those values are multiplied with a negative-mode amplitude for mode reconstruction (Figure 2B; yellow line). This results in positive values in the mode decay stack, calculated according to Equation (9) for $j = 0$ (Figure 2E, 'Mode 0'). Modes 1 and 2 describe the faster fluorescence loss in the nucleus and cytoplasm, while both modes have values close to zero for the aggregates (Figure 2B,D). This is confirmed for the reconstructed mode decays, calculated according to Equation (9) for $j = 1, 2$ (Figure 2E, middle and lower panels). In particular, one sees that the sum of modes 1 and 2 exactly reconstructs the nucleocytoplasmic exchange dynamics (Figure 2E lowest panel). The eigenvalues of mode 1 or 2 of the DMD (i.e., $\omega_1 = -0.0189$ and $\omega_2 = -0.1162$) are different from the eigenvalues describing the fluorescence-loss kinetics in the nucleus and cytoplasm in the FLIP simulations of Figure 2 ($l_2 = -0.6342$ and $l_3 = -0.01577$). The eigenvalues used in the simulations are comprised of a combination of all rate constants (l_2 and l_3 in the Appendix A, Equations (A8) and (A9)), and their fractional amplitude in the simulation corresponds to 4.9% and 78.1% for the second and third component, respectively. Thus, the first and third eigenfunctions comprise more than 95% of all decay in the simulation, with eigenvalues in close agreement with the DMD of the simulated FLIP series (i.e., $\omega_0 \approx l_1$ and $\omega_2 \approx l_3$, see Table 1). Similar observations were made for simulations with inert aggregates (i.e., no exchange with $l_1 = -k_2 \sim -0.00 \text{ s}^{-1}$). Thus, DMD identifies the dominant modes but eventually fails to identify small-amplitude contributions correctly. Moreover, the DMD reconstruction of additional simulations showed that the different combinations of rate constants cannot be uniquely assigned to the eigenvalues obtained by DMD. Only the first eigenvalue can be determined unequivocally in all cases, as this eigenvalue describes the release from the aggregates as a single-rate constant (see Equations (A5) and (A7)). The other two eigenvalues are a combination of rate constants (see Equations (A4) and (A6)), and it is well known that the non-orthogonality of exponential functions with real eigenvalues makes unequivocal identification of particular kinetic contributions difficult in such cases [53]. It should also be noted that our previous method of analyzing FLIP image sequences using pixel-wise fitting of exponential decay functions cannot unequivocally determine all eigenvalues of the simulated FLIP data either [11]. Fitting a bi-exponential decay model implemented in PixBleach to the FLIP simulation gave poor-fitting results (not shown).

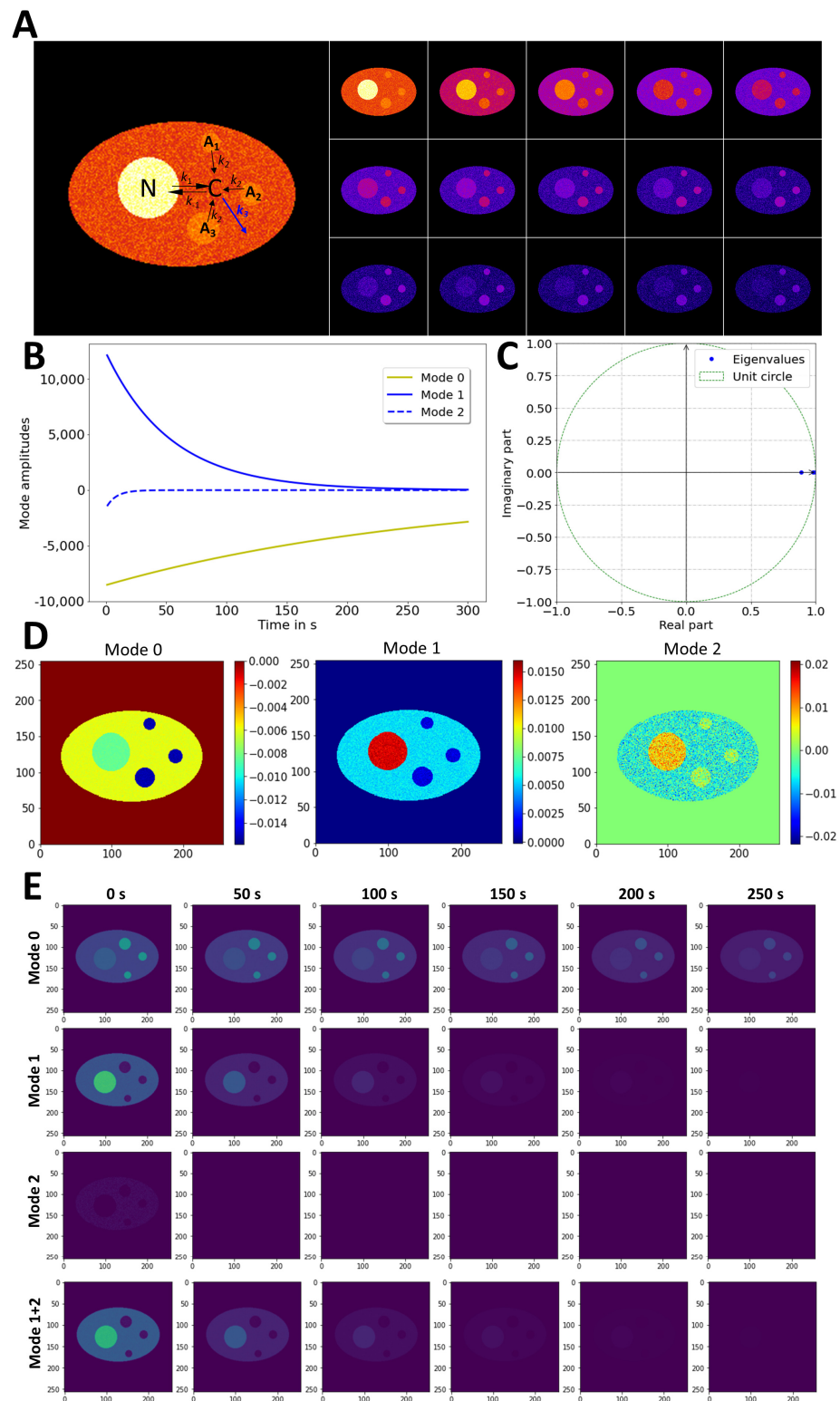


Figure 2. DMD of synthetic FLIP image series with cytoplasmic aggregates. Simulated FLIP images with nucleocyttoplasmic exchange (rate constants, k_1 and k_{-1}) and protein release from aggregates (rate constant k_2) as well as bleaching in the cytoplasm with rate constant k_3 (blue arrow, (A)). Montage of simulation with every 20th frame shown in left panel of (A,B), mode decays obtained by DMD of rank 3. (C) Eigenvalues plotted on unit circle. (D) The 2D maps of identified dynamic modes. (E) Reconstructed time evolution of each identified mode (upper three panels) and sum of mode 1 and 2 (lowest panel). See text for further explanations.

Table 1. Comparison of eigenvalues of FLIP simulation with estimated eigenvalues of DMD and pixel-wise exponential fitting.

Eigenvalues *	FLIP Simulation	DMD Reconstruction	Pixel-Wise Fitting #
$-k_2$	$l_1 = -0.0050 \text{ s}^{-1}$	$\omega_0 = -0.0038 \text{ s}^{-1}$	$k_{\text{agg.}} = -0.0051 \text{ s}^{-1}$
$-(2k_1 + k_3 + \sqrt{k_3^2 + 4k_1 \cdot k_{-1}})$	$l_2 = -0.6342 \text{ s}^{-1}$	$\omega_2 = -0.1162 \text{ s}^{-1}$	-
$-(2k_1 + k_3 - \sqrt{k_3^2 + 4k_1 \cdot k_{-1}})$	$l_3 = -0.0158 \text{ s}^{-1}$	$\omega_1 = -0.0189 \text{ s}^{-1}$	$k_{\text{cell.}} = -0.0139 \text{ s}^{-1}$

* Theoretical expression based on analytical FLIP model in Appendix A, Equations (A7)–(A9). # Determined using a stretched exponential function in PixBleach [11]. Rate constants were determined as inverse of the mean time constant values in the aggregates (k_{agg}) or the inverse of the averaged time constant values in the nucleus and cytoplasm (k_{cell}). The stretching parameter was $h = 0.999$, $h = 1.028$, and $h = 1.078$ in aggregates, nucleus, and cytoplasm, respectively.

Using a stretched exponential model, as in our previous study [11], only the first eigenvalue describing the release from the aggregates could be recovered precisely (Table 1).

It has to be emphasized, though, that DMD in its current implementation is not a fitting method, and the derived basis function does not necessarily represent the underlying biophysical mechanism. Possible extensions of the DMD method in future applications are considered in the Discussion section. Importantly, the reconstructed FLIP simulation calculated as a sum of all three modes resembles the original simulated image data very closely (Figure 3 and Supplementary Video S1). This can be inferred from the low and homogeneous square error between the simulation and the reconstruction (Figure 3A, right panels) as well as from the similar total-intensity decay (Figure 3B). It also becomes obvious that DMD efficiently denoises the FLIP image sequence, which is particularly important for later time points, when the majority of the signal is already removed (Figure 3A, lower panels). Note that the imaginary part of all modes was zero, as no intensity oscillations or lateral movement was considered in the FLIP simulation (not shown). In real experiments, aggregates might move slightly in the cells during a FLIP experiment, so the impact of the diffusion and flow of the aggregates on the DMD reconstruction quality was assessed as well. First, the random displacement of the smallest aggregate was included in the FLIP simulation. The Brownian motion of the aggregate could not be reconstructed by a low-rank DMD, which resulted in the blurring of the particle position (see Appendix B). Secondly, a directed movement component was added to the FLIP simulation to emulate diffusion with the flow of the smallest aggregate (Appendix B and Supplementary Video S2). In that case, the flow component without random motion was partially reconstructed by the DMD. Importantly, the fluorescence loss in the moving aggregates was still adequately described in both cases, showing that the decomposition of fluorescence-loss kinetics in the subcellular structure can be decoupled from the lateral displacement of those components.

3.2. DMD of Experimental FLIP Image Sequences of Nucleo-Cytoplasmic Exchange of eGFP

To assess the potential of DMD in the analysis of experimental FLIP image data, a FLIP experiment was carried out on McA cells expressing eGFP (see Materials and Methods). Repeated photobleaching of a small, circular regions in the cytoplasm caused the rapid fluorescence loss of eGFP. The fluorescence loss was first seen in the cytoplasm and, with a delay, also in the nucleus (Figure 4A). DMD of this data in PyDMD, using the optimal rank option, gave a rank-6 approximation of the data matrix, resulting in a very good reconstruction and denoising of the data (Figure 4A,B and Supplementary Video S3). Of note, the FLIP image stack reconstructed from DMD was significantly less noisy than the original data.

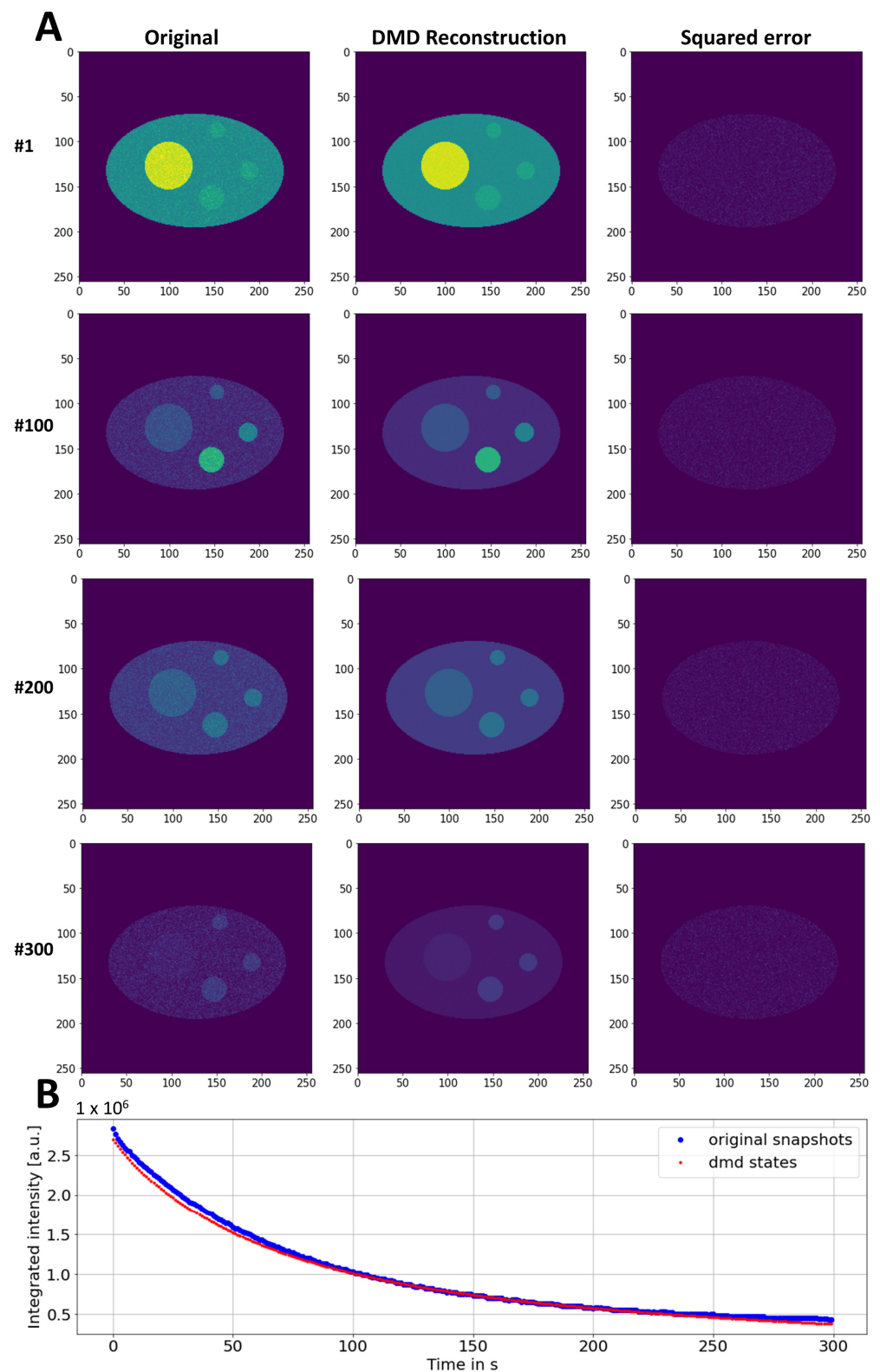


Figure 3. DMD reconstruction of synthetic FLIP images with decay in aggregates. (A) Comparison of simulated and DMD-reconstructed FLIP image series. The squared error with identical intensity scaling is shown in the right column. Legend at the left margin shows frame number ('#'). (B) Integrated intensity of simulated (blue dots) and reconstructed image series (red dots). See text for further explanations.

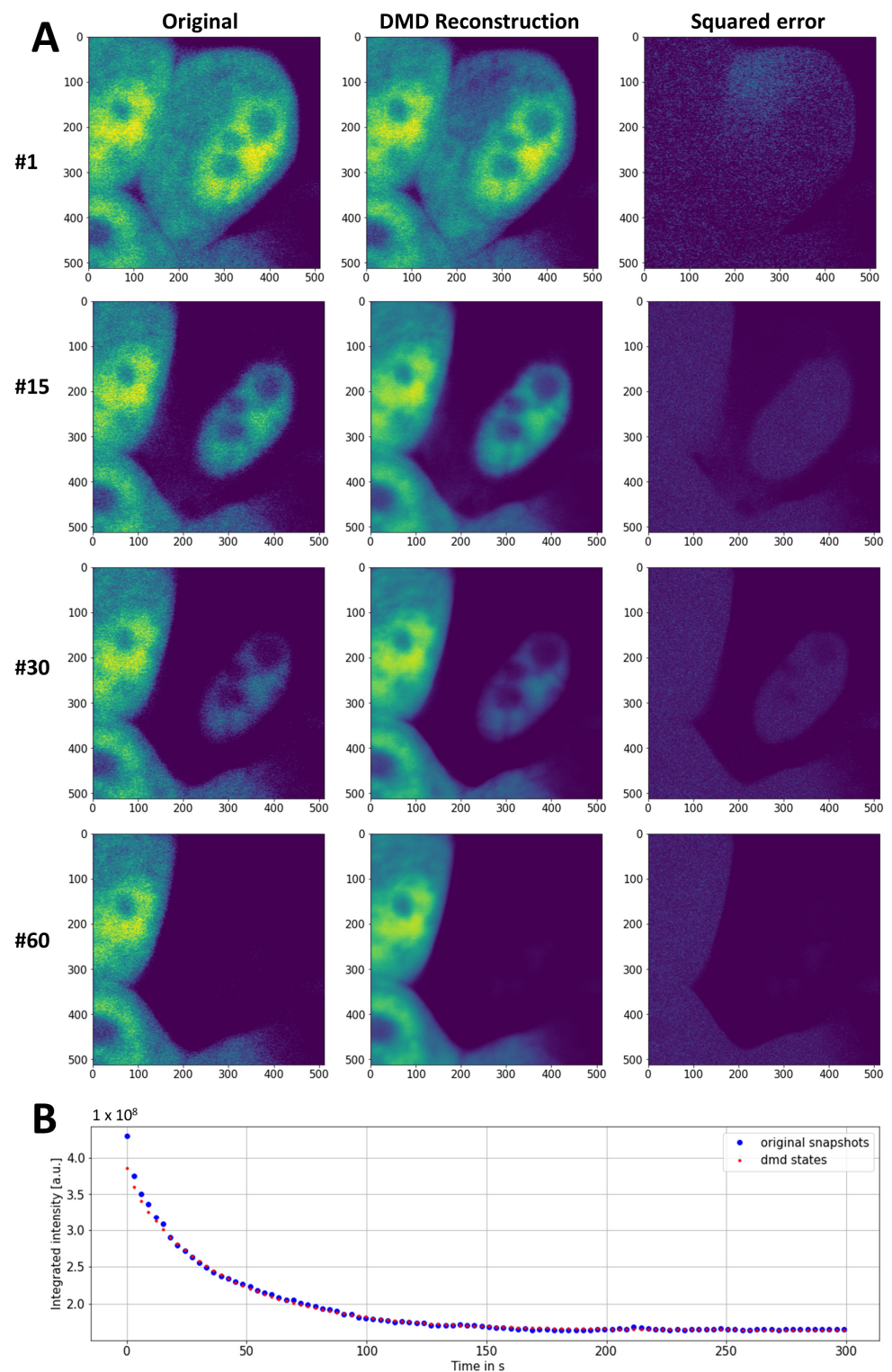


Figure 4. DMD reconstruction of experimental FLIP images of eGFP in McA cells. (A) FLIP experiment was carried out on a confocal microscope using McA cells expressing eGFP. Bleaching was performed in the cytoplasm every 3 sec, with image acquisition in between (see white circle in upper left panel for laser spot position in (A)). (A) Comparison of experimental and DMD-reconstructed FLIP image series. The squared error with identical intensity scaling is shown in the right column. Legend at the left margin shows frame number ('#'). (B) Integrated intensity of simulated (blue dots) and reconstructed image series (red dots). See text for further explanations.

The SVD of the space–time data matrix, corresponding to the entire FLIP image stack, revealed four dominant singular values that, together, contributed almost 90% of the data variance (Appendix C). Additionally, there was a slowly decaying contribution of more than 20 singular values, but the optimal rank was set to rank 6 using the hard-threshold algorithm of Gavish and Donoho (2014) [49]. The first two modes had amplitudes close to zero and were almost constant in time (Figure 5A) with no visible structure in the 2D-mode plots (not shown). The third mode could be assigned to the neighboring cell, which did not experience any fluorescence loss and, consequently, had a constant mode amplitude with an eigenvalue close to one ($\lambda_0 = 0.999$), corresponding to an eigenvalue of $\omega_0 = 0.00$ after rescaling to real time using Equation (8) (Figure 5A, green line, Figure 5B,C). Modes 3 to 5 described the fluorescence loss in the cytoplasm and nucleus with slowly decaying dynamics (Figure 5B green dashed line and red lines and Figure 5D–F). The small lateral displacements of the cell during the FLIP experiment are reflected in the non-zero imaginary contributions to modes 4 and 5 (Figure 5E,F). The reconstruction of the individual modes for this sequence, according to Equation (9), above, confirms that mode 2 accounts for the fluorescence of the unbleached neighboring cell, while modes 3 and 4 describe the fluorescence loss in the nucleus and cytoplasm (Appendix C). The results in Figures 4 and 5 demonstrate that DMD of live-cell FLIP image sequences allows for the efficient image denoising and the correct description of the pixel-wise fluorescence-loss dynamics in both compartments of bleached cells but also of fluorescence in the unbleached neighboring cells.

3.3. DMD of Experimental FLIP Image Sequences of Soluble and Aggregated eGFP-mtHtt

To assess the ability of DMD-FLIP to discern the dynamic components in FLIP experiments with protein aggregates, eGFP-tagged mtHtt, with a 145-residue long glutamine region (eGFP-Q145), was expressed in CHO cells. The FLIP microscopy of those cells revealed the existence of stable aggregates in which the protein exchange was significantly slowed (Figure 6A, upper panel). Faster-intensity decay was found in small, mobile aggregates. Fluorescence loss is only partial in the cell shown in Figure 6, as some out-of-focus drift made longer acquisitions unreliable. Still, DMD of this FLIP sequence resulted in a very good reconstruction with a close coincidence of the integrated intensity and significantly reduced noise levels (Figure 6A, lower panel and Figure 6B). The denoising capacity of DMD-FLIP is significant, as subcellular features are more discernable in the reconstructed stack than in the raw image sequence (6C–E). Denoising by DMD-FLIP is also efficient over time, where fluorescence-loss kinetics were much smoother in the reconstructed stack than in the original FLIP image data (Figure 6F,G). The temporal intensity profiles coincide well in regions with exponential fluorescence loss (Figure 6C,D, Box 1 to 3 and Figure 6F). Even the small protein aggregate highlighted in Box 1 showed significant fluorescence loss, which was adequately described by the DMD-reconstructed FLIP stack, with significant temporal denoising compared to the original FLIP data (compare the red and blue straight lines in Figure 6F, corresponding to Box 1 in Figure 6C,D). Only in regions of the large solid-like aggregate, where the intensity decay was minimal, DMD's intensity profile deviated somewhat from the experimental one (Figure 6C,D Box 4 and Figure 6G, dashed lines). This is likely due to the slow exchange and diffusion of proteins residing in the stable aggregates. The resulting non-exponential fluorescence loss is not adequately described by DMD. The extremely inefficient diffusion of eGFP-Q145 inside the aggregates was confirmed in separate FLIP experiments (Appendix D). The potential of DMD-FLIP to denoise FLIP image series is further demonstrated by comparison to other denoising algorithms, such as anisotropic filtering and PURE-LET denoising [54,55]. This analysis shows that DMD-FLIP is on par with (PURE-LET denoising) or even superior to (Anisotropic filtering) those methods (Appendix E). While PURE-LET denoising results in slightly higher PSNR than DMD-FLIP, the latter has a much better ability to denoise the time decay and to preserve fine structural details (Appendix E and see Supplementary Video S4). On the other hand, DMD-FLIP fails to accurately describe the sudden lateral displacement of small aggregates in the cell.

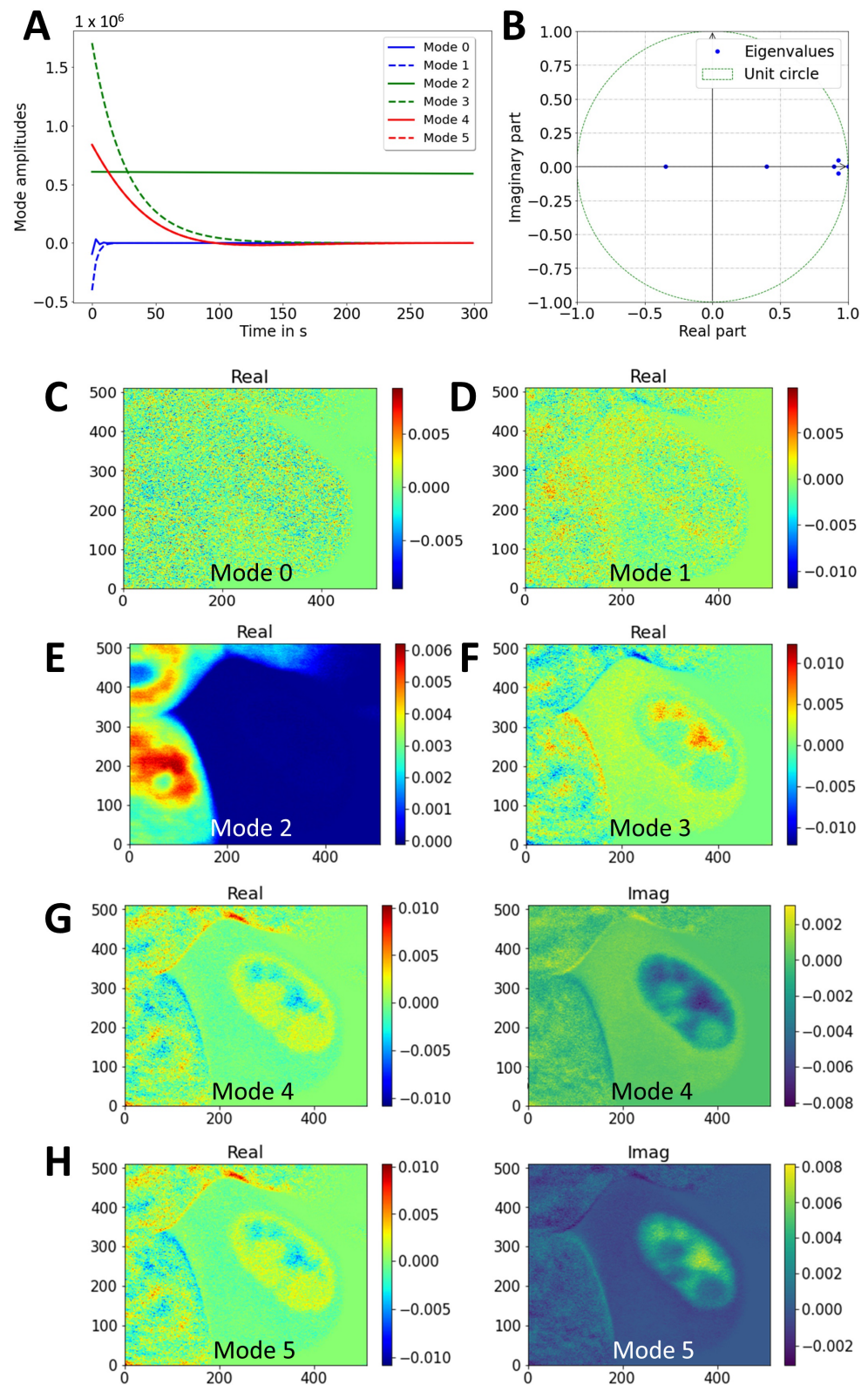


Figure 5. Analysis of DMD of FLIP image sequence of eGFP expressed in McA cells. (A) Mode decays obtained by DMD of experimental sequence from Figure 4 with rank 3. (B) Eigenvalues plotted on unit circle. (C–F) The 2D maps of the identified dynamic modes, i.e., real part of mode 0 (C), mode 1 (D), mode 2 (E), and mode 3 (F). All imaginary parts of those modes were zero (not shown). (G,H) Real and imaginary part of modes 4 (G) and 5 (H). Note that the mode images are flipped vertically compared to the original sequence (compare Figure 4). See text for further details.

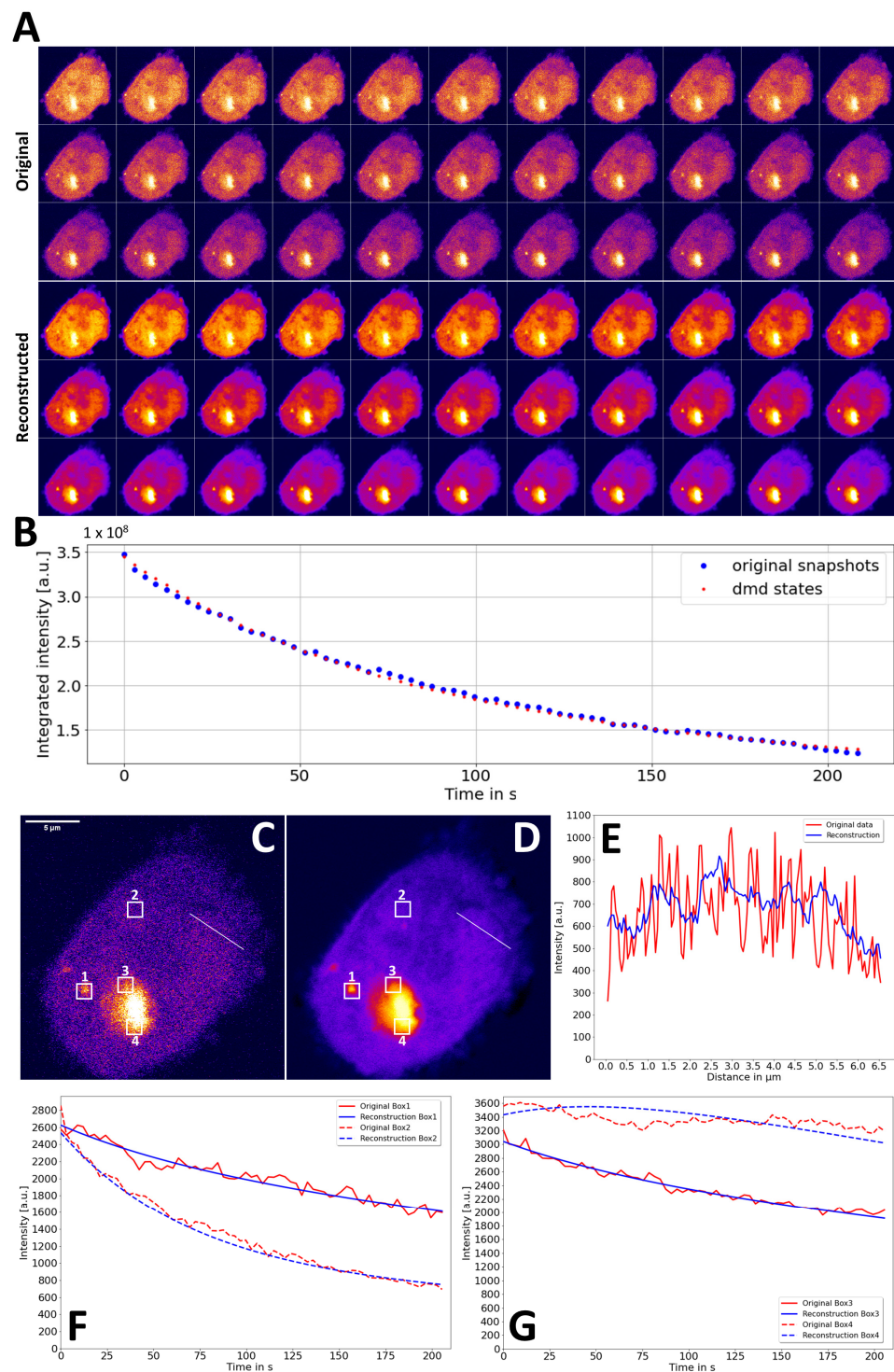


Figure 6. DMD reconstruction of experimental FLIP images of eGFP-Q145 expressed in CHO cells. A FLIP experiment was carried out on a confocal microscope using CHO cells expressing eGFP-Q145. Bleaching was performed in the cytoplasm every 3 s, with image acquisition in between (see white circle in upper left panel for laser spot position in (A)). (A) Comparison of original and DMD-reconstructed FLIP image series (every 2nd frame, i.e., every 6 s is shown). (B) Integrated intensity of experimental (blue dots) and reconstructed image series (red dots). (C,D) Last frame of original (C) and DMD-reconstructed (D) image stack with line and boxes indicated. E–G Line profile (E) along line in (C,D) and intensity time decay (F,G) for boxes indicated in (C,D) are shown. Original (red lines) and DMD-reconstructed (blue lines).

This is in line with the observations made in FLIP simulations with Brownian motion (see Appendices B and E). The optimal rank determined using the hard-thresholding method in PyDMD was rank = 2, since only two dominant singular values were found (Figure 7A). Thus, only two modes were considered in further analysis and used for image reconstruction. While mode 0 describes the slowly decaying fluorescence of eGFP-Q145 in cytoplasm and in the aggregates ($\omega_0 = -0.0051 \text{ s}^{-1}$), mode 1 comprises the faster decaying, likely monomeric or oligomeric, mobile eGFP-Q145 pool outside of aggregates (Figure 7C–E and Supplementary Video S5; $\omega_1 = -0.0443 \text{ s}^{-1}$). Thus, DMD-FLIP allows for the data-based discrimination of different dynamic pools of mtHtt in living cells. Apart from its efficient denoising capacity, this must be seen as one of the major strengths of this new method.

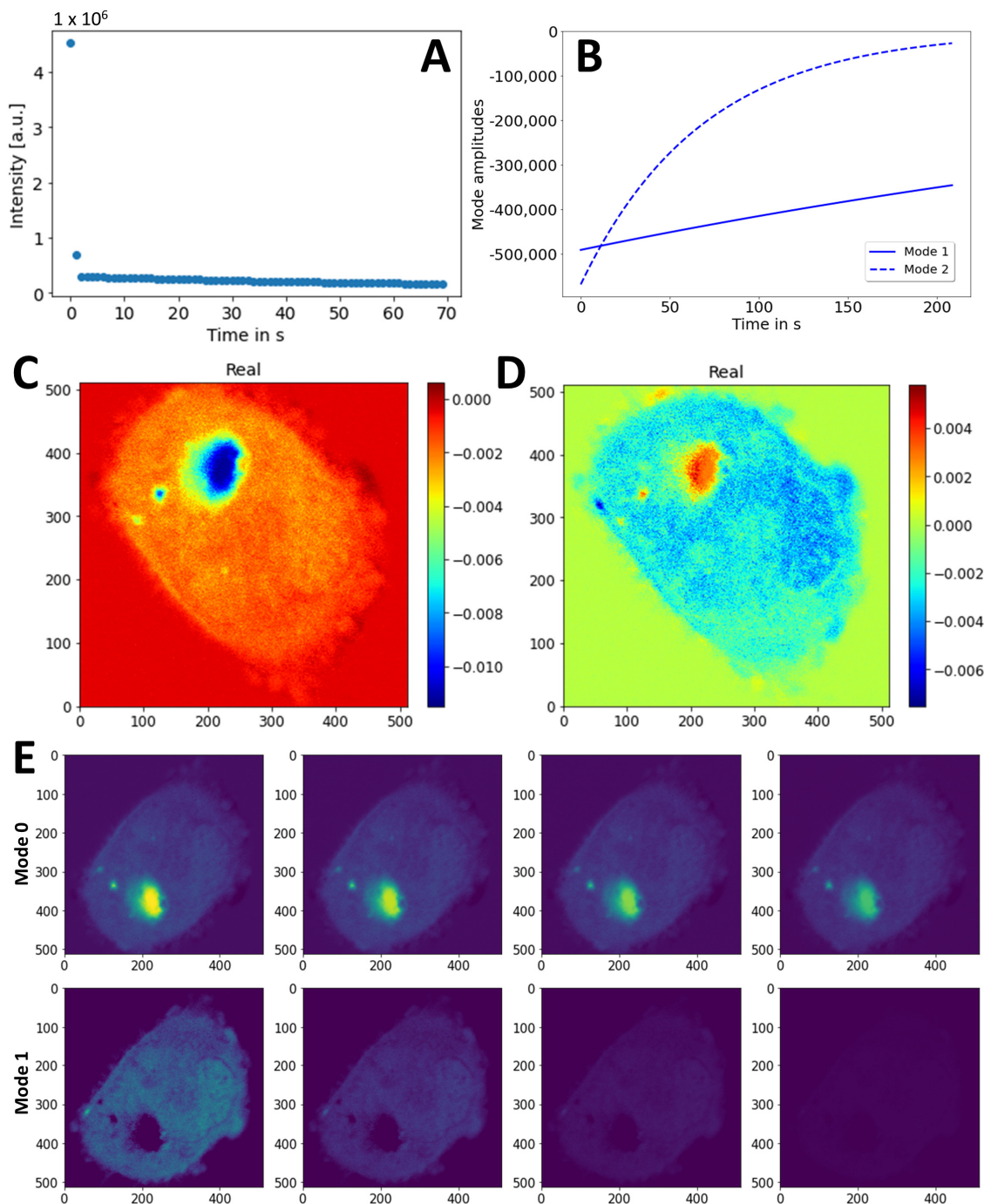


Figure 7. Analysis of DMD of FLIP image sequence of eGFP-Q145 expressed in CHO cells. (A) Singular

values calculated from reshaped image stack. (B) Mode decays obtained by DMD of experimental sequence from Figure 6 with rank 2. The 2D maps of real part of identified dynamic modes, with mode 0 (C), mode 1 (D). Imaginary parts were zero (not shown). (E) Reconstruction of mode 0, upper panel, and mode 1; lower panel with identical intensity scaling. Every 20th frame is shown; see text for further details.

4. Discussion

FLIP microscopy is widely employed to determine barriers to the diffusion of fluorescent proteins and other tagged biomolecules. When compared to FRAP, it has the important advantage of providing the cellular context, in which the diffusion, binding, and aggregation of proteins takes place. To make use of this potential, computational analysis of FLIP microscopy is of utmost importance for the proper interpretation of imaging data. In this study, a novel method is introduced, which allows for the dissection of the dynamic modes of fluorescence loss in FLIP live-cell-microscopy time-lapse data. Using simulated and experimental FLIP image sequences, it is shown that DMD-FLIP correctly identifies different dynamic contributions to the distinct fluorescence-loss signal in each compartment. DMD-FLIP employs the full range of spatiotemporal information available in the FLIP microscopy data to identify compartment-specific fluorescence-loss dynamics in the cytoplasm, nucleus, and in protein aggregates. It is, therefore, similar to coupled DMD, which has recently been successfully used in epidemiological multi-compartment systems [56]. Based on the determined time decay of fluorescence in aggregates, information about their physico-chemical properties can be inferred; while rapid fluorescence loss is found in liquid-like protein condensates, stable aggregates show very slow fluorescence decreases, due to hindered protein release. This is shown for eGFP-mtHtt, with an extended polyglutamine stretch (Figures 6 and 7). At the same time, DMD-FLIP is very efficient in denoising such FLIP image data, both in space (i.e., pixel-to-pixel variation in each image) and in time (i.e., intensity profiles in each pixel position). In this regard, DMD-FLIP is as effective as state-of-the-art denoising algorithms, such as PURE-LET denoising (Figure 7). DMD-FLIP can also be employed to predict the future images of a FLIP sequence, which may not yet have been acquired. This can potentially reduce the necessary light exposure required to infer intracellular transport dynamics in experiments.

The other computational FLIP microscopy techniques we developed previously comprise the pixel-wise fitting of a stretched exponential decay function to the FLIP image sequences and the reaction–diffusion modeling of protein transport and aggregation combined with model calibration to the experimental data [11,39,40]. DMD-FLIP complements these methods in several ways; first, it is model-free, circumventing the need for model assumptions. DMD-FLIP is, therefore, simple to implement for microscopists without extensive modeling experience. Secondly, DMD-FLIP is fast compared to those methods; it takes approximately 17 s to calculate DMD modes for the image sequence in Figures 6 and 7 on a zBook laptop computer and approximately 12 s on a modern desktop workstation (see Materials and Methods). Sequentially fitting a stretched exponential to each pixel (non-parallelized code) for the same image sequence on the same laptop machine takes 1862 s, i.e., more than 30 min, while it takes 290 s on a desktop workstation. Calibrating a full reaction–diffusion model for such data takes several hours on a desktop workstation [39]. Thus, DMD-FLIP is a much faster analysis method when compared to these techniques. It is also faster than PURE-Denoise.

Limitations of the current implementation of DMD-FLIP are, firstly, its inability to account properly for any abrupt lateral displacements of aggregates or other entities in the image sequence, such as those caused by Brownian motion (Figure A1). Secondly, the eigenfunctions derived by DMD are not always straightforward to associate with a particular physical process causing fluorescence loss in a given FLIP image sequence. Both limitations are inherently a result of the mathematical structure of the DMD framework; it seeks to find the best possible representation of the snapshots (i.e., images sampled in time) in a Fourier-like expansion of the eigenfunctions (Equation (8)). This does not neces-

sarily represent the physical model which has produced the snapshots [57]. For finding this representation, a linear, discrete, time-invariant process according to Equation (3) is assumed, lying in an invariant subspace under the action of the Koopman operator, thereby identifying coherent dynamic processes in the data. The learned or inferred eigenfunctions are, therefore, not necessarily identical to the ones producing the data [42,57]. This is illustrated for the DMD reconstruction of simulated FLIP image sequences, in which the determined eigenvalues only partially resemble the analytical model (Table 1), even though the reconstruction of the data is close to perfect (Figures 2 and 3). DMD is also not able to identify and describe abrupt intensity changes, such as changes in fluorescence transients or intensity oscillations or changes during stochastic particle movement, which are all examples of non-linear dynamics. The condition of linear dynamics, however, is met in FLIP image sequences, as long as no abrupt changes, such as those due to the diffusion of subcellular structures, either laterally or into and out of the focal plane of the objective, take place. In contrast, the directed movement (flow) of aggregates can be accounted for, to some degree, as shown in the simulations of Appendix B, and the experimental sequence in Appendix E (see also Supplementary Videos S1 and S5). This is also expected, as directed motion is highly correlated between frames, thereby resembling a coherent flow pattern, for which DMD was originally developed [41]. Increasing the rank of the DMD approximation of snapshots improved the reconstruction quality only slightly in those cases, but the stochastic component of the dynamics was still not properly described (not shown). It has to be emphasized, though, that neither pixel-based bleaching analysis nor our reaction–diffusion modeling of FLIP data can account for the sudden movement of subcellular structures [11,39,40].

5. Conclusions and Outlook

This study presents an easy-to-use computational method for the analysis of time-lapse FLIP imaging of living cells. DMD-FLIP accurately decomposes fluorescence-loss dynamics in various subcellular compartments, thereby allowing for the rapid and straightforward detection of barriers and obstacles to protein diffusion without the need for demanding modeling approaches. DMD-FLIP allows microscopists to efficiently denoise their FLIP-image data and to quickly obtain spatiotemporal maps of fluorescence-loss dynamics. The ability of DMD-FLIP to efficiently decompose the fluorescence-loss kinetics of different subcellular regions into distinct dynamic modes enables the study of protein dynamics at each time scale individually. This novel DMD-FLIP method is suitable for denoising spatiotemporal FLIP data for better visualization and further analysis. The reconstruction of partial FLIP data with incomplete fluorescence loss can enable optimization of FLIP experiments with minimal light exposure to reduce cell stress and prevent artefacts. DMD-FLIP also allows for the development of reduced models of intracellular dynamics and should thereby set the stage for the comprehensive modeling of protein transport and aggregation in living cells.

Several extensions of classical DMD can be considered to overcome the current limitations of DMD-FLIP in the future, which primarily include its inability to properly describe the abrupt translational motion of fluorescent entities and the accurate, but non-physical, description of kinetic data. Firstly, multiresolution DMD could be implemented, which allows for the improved description of dynamic modes at multiple and distinct time scales [44]. Secondly, physics-informed DMD should be employed to restrict the possible space of solutions to the minimization problem in Equation (4) to a subspace based on prior knowledge about the physical system under investigation [58]. This leads to a reformulation of the optimization task in DMD to a Procrustes problem, which could, for example, be used to model the convection–diffusion of aggregates or other subcellular structures in FLIP data via a tri-diagonal constraint to the admissible reconstruction of matrix A [58]. Another possibility to improve the analysis of FLIP, and other dynamic microscopy data, is to approximate the linear, but infinite, Koopman operator using non-linear measurement functions of the state variable x , as performed in extended dynamic mode decomposition [59].

This would potentially also allow for the description of a combination of stochastic and deterministic dynamics, as is often encountered in live-cell time-lapse microscopy. The ultimate goal of data-driven modeling of microscopy data is to infer the real underlying equations governing the experimentally observed dynamics. This has been attempted by calibrating multi-compartment, reaction–diffusion systems in our previous studies [7,39,40]. A very attractive strategy would be to attempt to discover and parametrize such equations directly from the data, including an account for protein diffusion using sparse identification strategies of the underlying partial differential equations [60]. This will be the focus of future research.

Supplementary Materials: The following supporting information can be downloaded at: <https://www.mdpi.com/article/10.3390/s22134731/s1>, Video S1: Supplementary_video_1.avi, Video S2: Supplementary_video_2.avi, Video 3: Supplementary_video_3.avi, Video 4: Supplementary_video_4.avi. **Supplementary video sequences: Supplementary Video S1. Comparison of FLIP simulation and DMD reconstruction.** Synthetic FLIP sequence of Figure 1 is compared to the corresponding DMD reconstruction. The sequence was compressed in JPEG format and played at 10 fps. Note that the images are vertically flipped compared to the main figure. A FIRE LUT is used for intensity calibration. Images are scaled identically. **Supplementary Video S2. Comparison of FLIP simulation with diffusion + flow and its DMD reconstruction.** Synthetic FLIP sequence of Figure A1B is compared to the corresponding DMD reconstruction. The sequence was compressed in JPEG format and played at 10 fps. Note that the images are vertically flipped compared to the main figure. A FIRE LUT is used for intensity calibration. Images are scaled identically. **Supplementary Video S3. Comparison of experimental FLIP sequence of eGFP and its DMD reconstruction.** Experimental FLIP of eGFP in McA cells of Figure 4 is compared to the corresponding DMD reconstruction. The sequence was compressed in JPEG format and played at 10 fps. Note that the images are vertically flipped compared to the main figure. A FIRE LUT is used for intensity calibration. Images are scaled identically. **Supplementary Video S4. Comparison of denoising methods applied to experimental FLIP sequence of eGFP-Q145.** Experimental FLIP of eGFP-Q145 in CHO cells of Figures 6 and 7 ('Original', upper left sequence) is compared to its DMD reconstruction (upper-right sequence), to anisotropic diffusion (lower left sequence) and to PURE denoising (lower-right sequence). The sequence was compressed in JPEG format and played at 10 fps. A FIRE LUT is used for intensity calibration. Images are scaled identically. **Supplementary Video S5. DMD reconstruction of experimental FLIP sequence of eGFP-Q145.** Experimental FLIP of eGFP-Q145 in CHO cells was used for DMD reconstruction, as shown in Figures 6 and 7, with two dynamic modes identified. DMD reconstruction (left sequence) is compared to reconstructed mode 0 (middle panel) and mode 1 (right panel). Note that mode 0 shows very slow decay including the aggregates, while mode 1 shows faster decay in all cellular regions except the aggregates (compare Figure 7E). The video sequence was compressed in JPEG format and played at 10 fps. A FIRE LUT is used for intensity calibration. Images are scaled identically.

Funding: This work was funded by the Villum foundation (Villum Fonden, Grant nr.: 35865).

Institutional Review Board Statement: Not applicable.

Informed Consent Statement: Not applicable.

Data Availability Statement: All data analyzed during this study are included in this published article [and its supplementary information files]. The original datasets generated and/or analyzed during the current study are available in the GITHUB repository, DanielW-alt/DMD-FLIP (github.com).

Acknowledgments: D.W. acknowledges technical assistance from Tanja Christensen, BMB, SDU, Denmark and thanks the Villum Foundation for supporting this work.

Conflicts of Interest: The authors declare no conflict of interest. The funders had no role in the design of the study; in the collection, analyses, or interpretation of data; in the writing of the manuscript, or in the decision to publish the results.

Appendix A. Derivation of Analytical Solution for FLIP Simulation

Here, the analytical FLIP model used in the simulations described in Figures 2 and 3 is derived. The model assumes a linear relationship between the measured fluorescence signal and the concentration of tagged protein in cells, i.e., the fluorescence saturation or photobleaching of labeled protein during image acquisition are neglected. Both assumptions are reasonable, as long as the intensity of the excitation laser is low compared to the rate constants of the photocycle of the eGFP fluorophore [61,62]. Three dynamic populations of the tagged protein are considered: protein in the nucleus, $N(t)$, in the cytoplasm, $C(t)$, and in the aggregates/inclusion bodies, $A(t)$. While the exchange between the nucleus and the cytoplasm is bidirectional with a forward rate constant, k_1 , and a backward rate constant, k_{-1} , the protein release from the aggregate is assumed to be irreversible and identical for several aggregates, such that only a release rate constant, k_2 , is considered. Finally, the protein is assumed to be bleached in FLIP experiments in the cytoplasm with a rate constant k_3 . Diffusion is assumed to be much faster than all transport steps, such that it is ignored, and well-mixed conditions are assumed. This leads to the following ordinary differential equation system (see also Figure 2A):

$$\frac{dN}{dt} = -k_1 \cdot N + k_{-1} \cdot C \quad (\text{A1})$$

$$\frac{dA}{dt} = -k_2 \cdot A \quad (\text{A2})$$

$$\frac{dC}{dt} = k_1 \cdot N - (k_{-1} + k_3) \cdot C + k_2 \cdot A \quad (\text{A3})$$

The system can be solved analytically by calculating the eigenvalues and eigenvectors of the underlying system matrix using Mathematica (Wolfram Research), as shown previously for similar systems [11,61,63]. This gives the following solution:

$$N(t) = c_{11} \cdot a_1 \cdot e^{l_1 \cdot t} + c_{21} \cdot a_2 \cdot e^{l_2 \cdot t} + c_{31} \cdot a_3 \cdot e^{l_3 \cdot t} \quad (\text{A4})$$

$$A(t) = c_{12} \cdot a_1 \cdot e^{l_1 \cdot t} + c_{22} \cdot a_2 \cdot e^{l_2 \cdot t} + c_{32} \cdot a_3 \cdot e^{l_3 \cdot t} \quad (\text{A5})$$

$$C(t) = c_{13} \cdot a_1 \cdot e^{l_1 \cdot t} + c_{23} \cdot a_2 \cdot e^{l_2 \cdot t} + c_{33} \cdot a_3 \cdot e^{l_3 \cdot t} \quad (\text{A6})$$

The eigenvalues of this solution are:

$$l_1 = -k_2 \quad (\text{A7})$$

$$l_2 = -(2k_1 + k_3 + \sqrt{k_3^2 + 4k_1 \cdot k_{-1}}) \quad (\text{A8})$$

$$l_3 = -(2k_1 + k_3 - \sqrt{k_3^2 + 4k_1 \cdot k_{-1}}) \quad (\text{A9})$$

In addition, the corresponding eigenvectors which form the basis set for the decoupled system read:

$$\begin{aligned} \bar{c}_1 &= (c_{11}, c_{12}, c_{13})^T \\ &= \left(\frac{k_{-1}}{k_1 - k_2}, \frac{k_1^2 + k_2 \cdot (k_2 - k_3) + k_1 \cdot (-2k_2 + k_3 - k_{-1})}{k_2 \cdot (k_2 - k_1)}, 1 \right) \end{aligned} \quad (\text{A10})$$

$$\bar{c}_2 = (c_{21}, c_{22}, c_{23})^T = \left(-\frac{-k_3 + \sqrt{k_3^2 + 4k_1 \cdot k_{-1}}}{2k_1}, 0, 1 \right) \quad (\text{A11})$$

$$\bar{c}_3 = (c_{31}, c_{32}, c_{33})^T = \left(-\frac{-k_3 - \sqrt{k_3^2 + 4k_1 \cdot k_{-1}}}{2k_1}, 0, 1 \right) \quad (\text{A12})$$

The integration constants a_1, a_2, a_3 , are calculated using the initial intensities in the nucleus, N_0 , the cytoplasm, C_0 , and the aggregates, A_0 , from Equations (A4)–(A6) for $t = 0$ and read:

$$a_1 = \frac{A_0}{c_{12}} \quad (\text{A13})$$

$$a_2 = \frac{c_{31} \cdot C_0 + (c_{11} - c_{31}) \cdot \frac{A_0}{c_{12}} - N_0}{c_{31} - c_{21}} \quad (\text{A14})$$

$$a_3 = C_0 - (a_1 + a_2) \quad (\text{A15})$$

The system solutions were plotted for each pixel in all of the three compartments as described in the Materials and Methods section.

Appendix B. FLIP Simulation with Moving Aggregates and Their DMD Reconstruction

FLIP simulations were carried out as described in the Materials and Methods section using the analytical solution of the FLIP model shown in Appendix A. However, in contrast to the simulations shown in Figure 1, the smallest of the three aggregates was allowed to move between frames by slow diffusion (Figure A1A) or by slow diffusion + flow (Figure A1B).

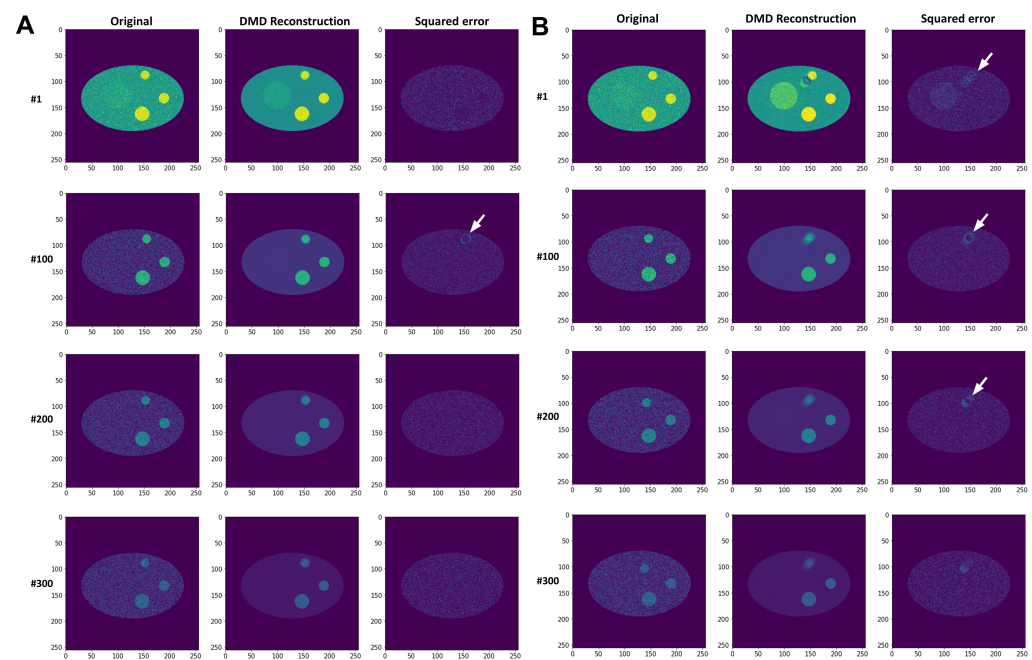


Figure A1. DMD reconstruction of synthetic FLIP images with decay in moving aggregates. Comparison of simulated and DMD-reconstructed FLIP image series, in which the smallest upper aggregate undergoes Brownian motion (i.e., normal diffusion, (A)) or diffusion + flow (B). The squared error with identical intensity scaling is shown in the right columns of each panel and reveals that aggregate displacements are not properly reconstructed by DMD (arrows).

One sees from Figure A1, that DMD fails to properly account for small stochastic displacements. Moreover, DMD does not reconstruct the diffusion + flow of the small aggregate correctly. Intensity decays, however, are correctly recovered, exactly as in the simulation without particle movement (compare to Figure 1).

Appendix C. Singular Values and Mode Reconstruction of Experimental FLIP Sequence

The DMD of the experimental FLIP sequence of eGFP in McA cells provided six dynamic modes based on the optimal threshold method developed by Gavish and Donoho [49]; see Materials and Methods. As shown in Figure A2A, the SVD of the data matrix corresponding to the experimental FLIP image stack revealed three dominant singular values. The next three singular values had slightly higher values than the subsequent ones and were also included in the analysis. The dynamic modes corresponding to the non-bleaching fluorescence of the neighbor cells (Mode 2) and of fluorescence loss of eGFP in nucleus and cytoplasm of the bleached cell are shown in Figure A2B.

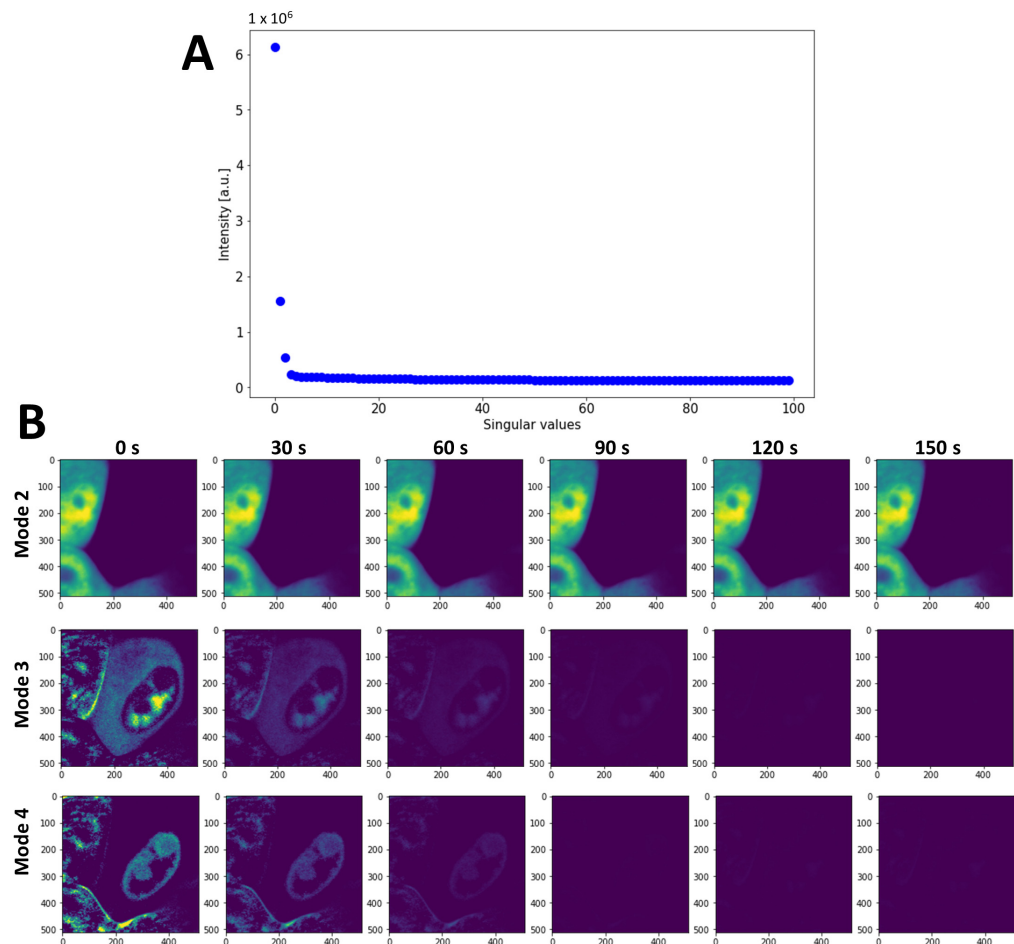


Figure A2. Singular values and selected mode reconstructions of experimental FLIP images of eGFP. Singular values (A) and reconstructed mode (B). Modes are shown for neighbor cells not experiencing fluorescence loss ('Mode 2') and for the bleached cell with fluorescence loss in cytoplasm and nucleus ('Mode 3 and 4').

Appendix D. Solid-Like Properties of Large eGFP-Q145 Aggregates Determined by FLIP

It has been shown that proteins in liquid-like aggregates can not only exchange rapidly with their local environment, but can also diffuse inside the protein condensates [26]. This is in contrast to solid-like aggregates, in which diffusion is very much slowed. Using FLIP with the bleaching laser placed on top of a large aggregate in CHO cells expressing eGFP-Q145, it is shown that this aggregate has a solid-like character. This can be inferred from the absence of diffusional spreading upon bleaching the aggregate, very much as we observed previously for eGFP in cells fixed with paraformaldehyde [11]. Similar observations were made for other cells with large aggregates of eGFP-Q145 (not shown).

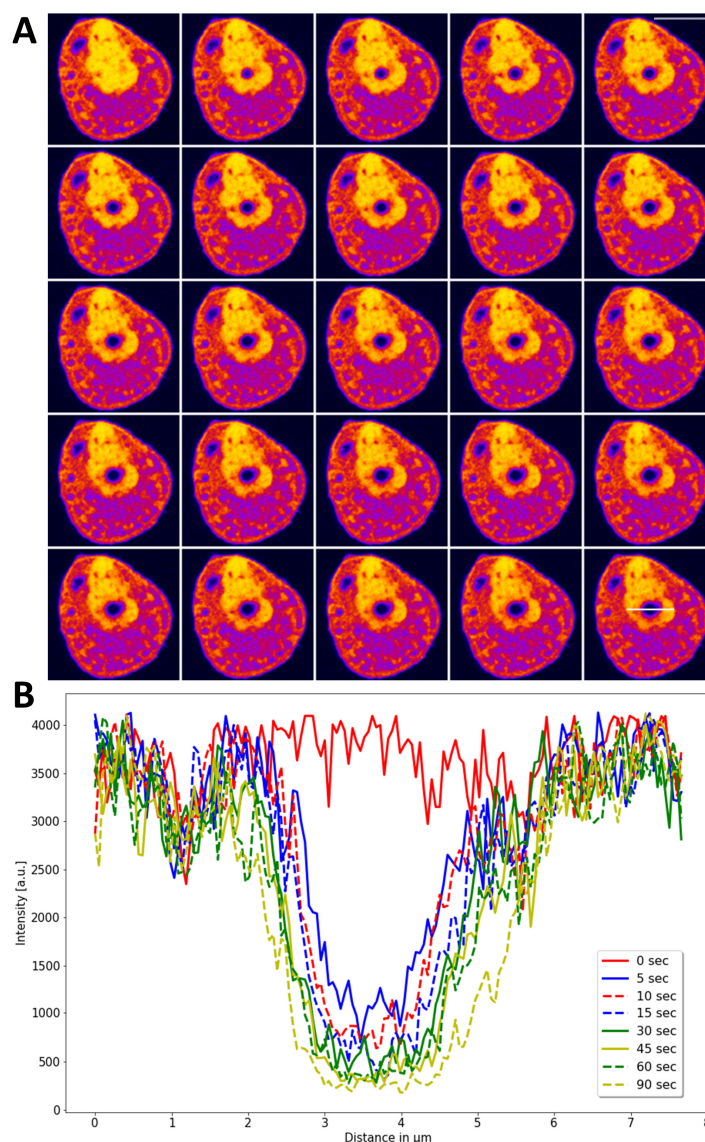


Figure A3. FLIP of eGFP-mtHtt aggregates reveal their solid-like character. CHO cells expressing eGFP-Q145 were repeatedly bleached at the aggregate position with image acquisition every 5 s (every 3rd image is shown in (A)). Images are identically scaled using a FIRE LUT. Bar, 10 μm . (B), measuring intensity of eGFP-Q145 along a line across the bleach spot (indicated as white line in last panel in (A)) revealed the absence of diffusional spreading, ruling out that significant diffusion takes place inside the aggregate. Supporting this notion, no fluorescence loss outside of the aggregate was found. Similar results were found for other aggregates (not shown).

Appendix E. Comparison of Image Denoising Potential of DMD-FLIP Compared to Other Methods

The denoising ability of DMD FLIP was compared to two established methods, Anisotropic Filtering and PURE-LET denoising, both being implemented as plugins to Image J (Figures A4 and A5) [54,55]. Clearly, DMD-FLIP and PURE-LET denoising perform best and comparably with respect to lateral denoising of images, while anisotropic diffusion shows worse performance. When comparing the abilities of all methods to denoise along the time axis, i.e., for temporal denoising, DMD-FLIP removed all intensity fluctuations (Figure 6), while anisotropic diffusion could not denoise fluorescence loss profiles at all (not shown).

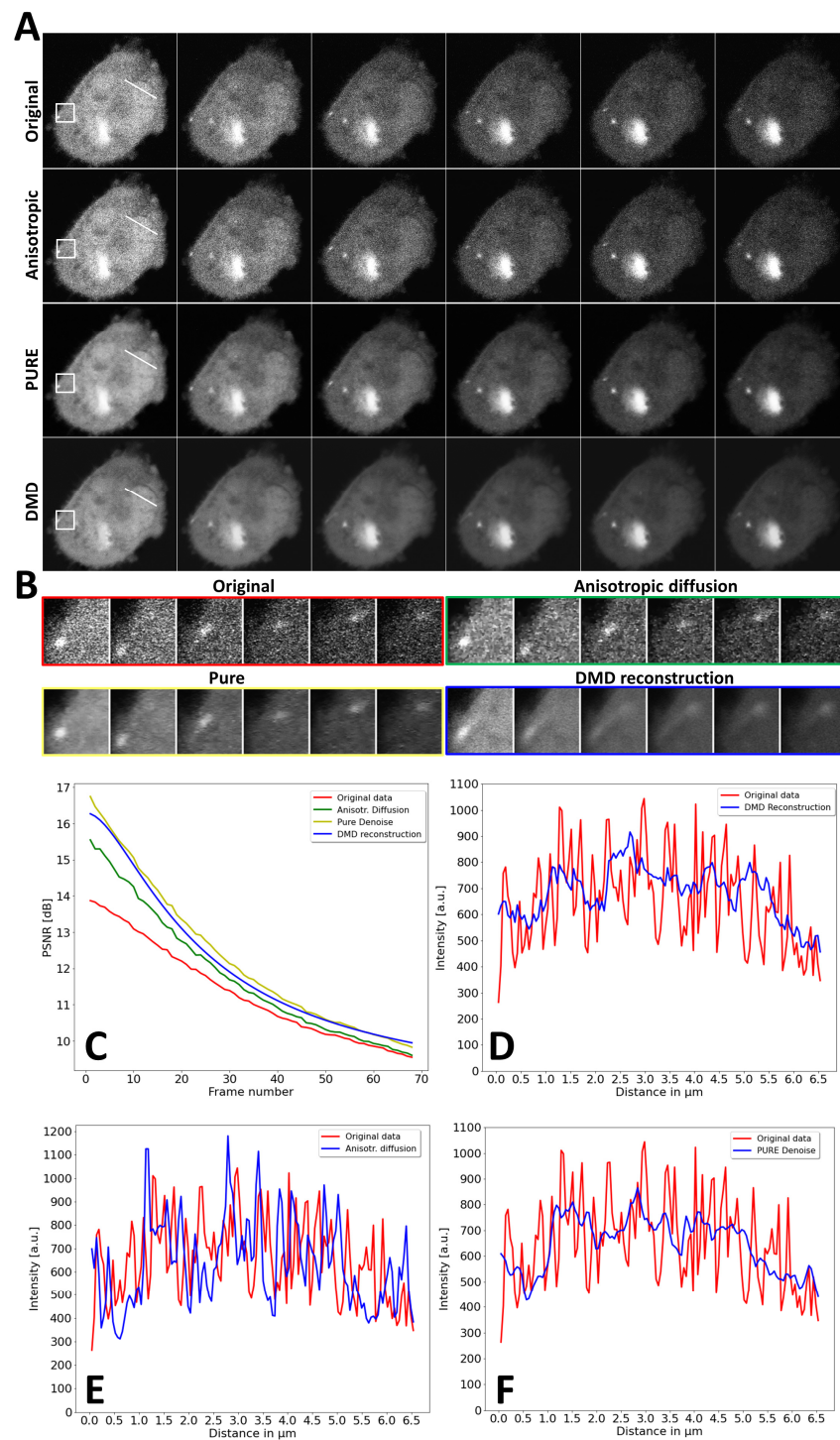


Figure A4. Denoising capacity of DMD-FLIP compared to other methods. FLIP image series of CHO cells expressing eGFP-Q145 from Figures 6 and 7 of the main text was compared to anisotropic diffusion (Anisotr. diffusion) and PURE-LET denoising (Pure Denoise/PURE). (A) The 1st row shows raw data, 2nd row is Anisotr. diffusion, 3rd row is Pure Denoise, and 4th row is DMD-FLIP reconstruction. (B) The box from A shows small aggregate moving from the lower left to the upper right corner of the box for the different denoising methods. (C) The peak signal-to-noise ratio (PSNR) in decibel for original data (red line), Anisotr. diffusion (green line), DMD-FLIP (blue line), and Pure Denoise (yellow line) with the first raw image as reference and as function of frames in the FLIP stack. D-F, intensity profile along line in A for original data (red line), for DMD-FLIP (blue line in (D)), Anisotr. diffusion (blue line in (E)), and Pure Denoise (blue line in (F)).

PURE denoising reduced sudden intensity fluctuations only minimally (Figure A5, below).

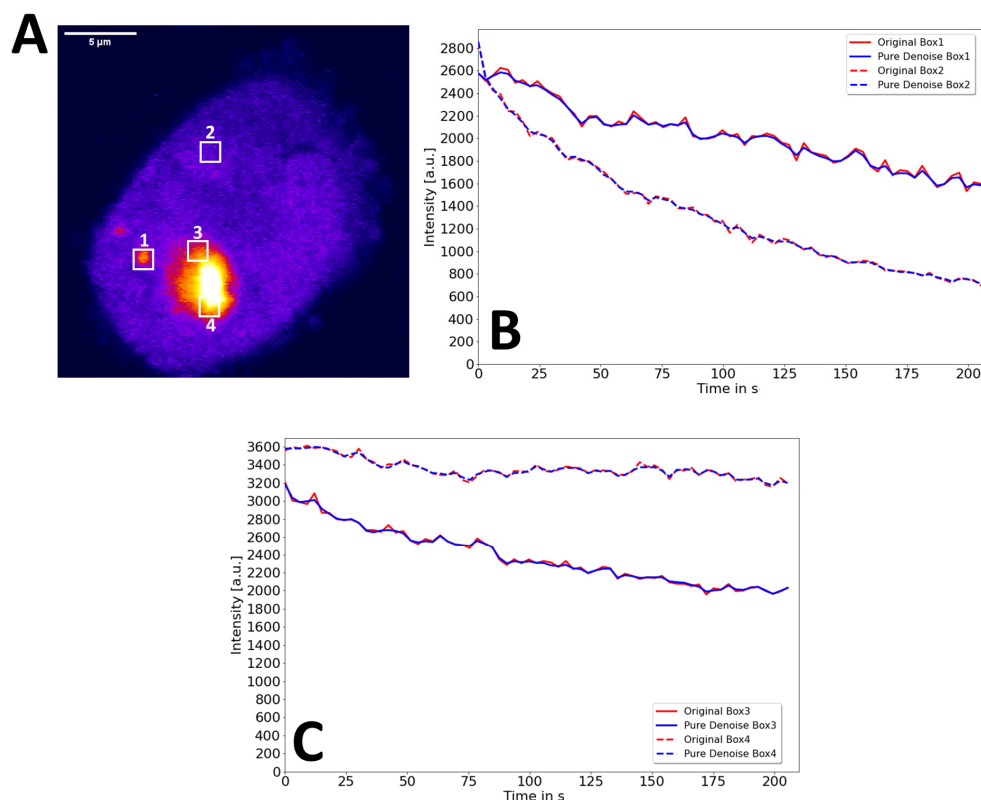


Figure A5. Temporal denoising of experimental FLIP image sequence by PURE-LET denoising. FLIP image sequence of eGFP-Q145 (see Figures 6, 7 and A4) was denoised using the PURE-LET method and intensity profiles along the time axis were analyzed as described in Figure 6 for DMD-FLIP. (A) Image frame of FLIP sequence with boxes indicated (compare Fig. 6D). Mean intensity in the white boxes of panel (A) were analyzed for PURE denoising (blue lines) and original image stacks (red lines) for boxes 1 and 2 (B) and for boxes 3 and 4 (C).

References

1. Sprague, B.L.; McNally, J.G. FRAP analysis of binding: Proper and fitting. *Trends Cell Biol.* **2005**, *15*, 84–91. [[CrossRef](#)] [[PubMed](#)]
2. Reits, E.A.; Neeffjes, J.J. From fixed to FRAP: Measuring protein mobility and activity in living cells. *Nat. Cell Biol.* **2001**, *3*, E145–E147. [[CrossRef](#)] [[PubMed](#)]
3. Ishikawa-Ankerhold, H.C.; Ankerhold, R.; Drummen, G.P. Advanced fluorescence microscopy techniques—FRAP, FLIP, FLAP, FRET and FLIM. *Molecules* **2012**, *17*, 4047–4132. [[CrossRef](#)] [[PubMed](#)]
4. Bancaud, A.; Huet, S.; Daigle, N.; Mozziconacci, J.; Beaudouin, J.; Ellenberg, J. Molecular crowding affects diffusion and binding of nuclear proteins in heterochromatin and reveals the fractal organization of chromatin. *EMBO J.* **2009**, *28*, 3785–3798. [[CrossRef](#)] [[PubMed](#)]
5. Gura Sadovskiy, R.; Brielle, S.; Kaganovich, D.; England, J.L. Measurement of Rapid Protein Diffusion in the Cytoplasm by Photo-Converted Intensity Profile Expansion. *Cell Rep.* **2017**, *18*, 2795–2806. [[CrossRef](#)]
6. Müller, F.; Mazza, D.; Stasevich, T.J.; McNally, J.G. FRAP and kinetic modeling in the analysis of nuclear protein dynamics: What do we really know? *Curr. Opin. Cell Biol.* **2010**, *22*, 403–411. [[CrossRef](#)]
7. Hansen, C.V.; Schroll, H.J.; Wüstner, D. Computational modeling of fluorescence loss in photobleaching. *Comput. Vis. Sci.* **2015**, *17*, 151–166. [[CrossRef](#)]
8. Stasevich, T.J.; Mueller, F.; Michelman-Ribeiro, A.; Rosales, T.; Knutson, J.R.; McNally, J.G. Cross-validating FRAP and FCS to quantify the impact of photobleaching on in vivo binding estimates. *Biophys. J.* **2010**, *99*, 3093–3101. [[CrossRef](#)]
9. Mazza, D.; Mueller, F.; Stasevich, T.J.; McNally, J.G. Convergence of chromatin binding estimates in live cells. *Nat. Methods* **2013**, *10*, 691–692. [[CrossRef](#)]
10. Mazza, D.; Abernathy, A.; Golob, N.; Morisaki, T.; McNally, J.G. A benchmark for chromatin binding measurements in live cells. *Nucleic Acids Res.* **2012**, *40*, e119. [[CrossRef](#)]
11. Wüstner, D.; Solanko, L.M.; Lund, F.W.; Sage, D.; Schroll, J.A.; Lomholt, M.A. Quantitative fluorescence loss in photobleaching for analysis of protein transport and aggregation. *BMC Bioinform.* **2012**, *13*, 296. [[CrossRef](#)] [[PubMed](#)]

12. Nicholson, L.; Gervasi, N.; Falieres, T.; Leroy, A.; Miremont, D.; Zala, D.; Hanus, C. Whole-Cell Photobleaching Reveals Time-Dependent Compartmentalization of Soluble Proteins by the Axon Initial Segment. *Front. Cell Neurosci.* **2020**, *14*, 180. [[CrossRef](#)] [[PubMed](#)]
13. Digman, M.A.; Gratton, E. Imaging barriers to diffusion by pair correlation functions. *Biophys. J.* **2009**, *97*, 665–673. [[CrossRef](#)] [[PubMed](#)]
14. Hinde, E.; Cardarelli, F.; Digman, M.A.; Gratton, E. In vivo pair correlation analysis of EGFP intranuclear diffusion reveals DNA-dependent molecular flow. *Proc. Natl. Acad. Sci. USA* **2010**, *107*, 16560–16565. [[CrossRef](#)]
15. Cardarelli, F.; Gratton, E. In vivo imaging of single-molecule translocation through nuclear pore complexes by pair correlation functions. *PLoS ONE* **2010**, *5*, e10475. [[CrossRef](#)]
16. Di Rienzo, C.; Cardarelli, F.; Di Luca, M.; Beltram, F.; Gratton, E. Diffusion Tensor Analysis by Two-Dimensional Pair Correlation of Fluorescence Fluctuations in Cells. *Biophys. J.* **2016**, *111*, 841–851. [[CrossRef](#)]
17. Malacrida, L.; Hedde, P.N.; Ranjit, S.; Cardarelli, F.; Gratton, E. Visualization of barriers and obstacles to molecular diffusion in live cells by spatial pair-cross-correlation in two dimensions. *Biomed. Opt. Express.* **2018**, *9*, 303–321. [[CrossRef](#)]
18. Bracha, D.; Walls, M.T.; Brangwynne, C.P. Probing and engineering liquid-phase organelles. *Nat. Biotechnol.* **2019**, *37*, 1435–1445. [[CrossRef](#)]
19. Zbinden, A.; Perez-Berlanga, M.; De Rossi, P.; Polymenidou, M. Phase Separation and Neurodegenerative Diseases: A Disturbance in the Force. *Dev. Cell* **2020**, *55*, 45–68. [[CrossRef](#)]
20. Kim, S.; Nollen, E.A.; Kitagawa, K.; Bindokas, V.P.; Morimoto, R.I. Polyglutamine protein aggregates are dynamic. *Nat. Cell Biol.* **2002**, *4*, 826–831. [[CrossRef](#)]
21. Matsumoto, G.; Kim, S.; Morimoto, R.I. Huntingtin and mutant SOD1 form aggregate structures with distinct molecular properties in human cells. *J. Biol. Chem.* **2006**, *281*, 4477–4485. [[CrossRef](#)] [[PubMed](#)]
22. Chai, Y.; Shao, J.; Miller, V.M.; Williams, A.; Paulson, H.L. Live-cell imaging reveals divergent intracellular dynamics of polyglutamine disease proteins and supports a sequestration model of pathogenesis. *Proc. Natl. Acad. Sci. USA* **2002**, *99*, 9310–9315. [[CrossRef](#)] [[PubMed](#)]
23. Irwin, S.; Vandelft, M.; Pinchev, D.; Howell, J.L.; Graczyk, J.; Orr, H.T.; Truant, R. RNA association and nucleocytoplasmic shuttling by ataxin-1. *J. Cell Sci.* **2005**, *118 Pt 1*, 233–242. [[CrossRef](#)]
24. Krol, H.A.; Krawczyk, P.M.; Bosch, K.S.; Aten, J.A.; Hol, E.M.; Reits, E.A. Polyglutamine expansion accelerates the dynamics of ataxin-1 and does not result in aggregate formation. *PLoS ONE* **2008**, *3*, e1503. [[CrossRef](#)] [[PubMed](#)]
25. Lajoie, P.; Snapp, E.L. Formation and toxicity of soluble polyglutamine oligomers in living cells. *PLoS ONE* **2010**, *5*, e15245. [[CrossRef](#)]
26. Peskett, T.R.; Rau, F.; O'Driscoll, J.; Patani, R.; Lowe, A.R.; Saibil, H.R. A Liquid to Solid Phase Transition Underlying Pathological Huntingtin Exon1 Aggregation. *Mol. Cell* **2018**, *70*, 588–601.e6. [[CrossRef](#)]
27. Elbaum-Garfinkle, S. Matter over mind: Liquid phase separation and neurodegeneration. *J. Biol. Chem.* **2019**, *294*, 7160–7168. [[CrossRef](#)]
28. Stenoien, D.L.; Mielke, M.; Mancini, M.A. Intranuclear ataxin1 inclusions contain both fast- and slow-exchanging components. *Nat. Cell Biol.* **2002**, *4*, 806–810. [[CrossRef](#)]
29. Kitamura, A.; Kubota, H.; Pack, C.G.; Matsumoto, G.; Hirayama, S.; Takahashi, Y.; Kimura, H.; Kinjo, M.; Morimoto, R.I.; Nagata, K. Cytosolic chaperonin prevents polyglutamine toxicity with altering the aggregation state. *Nat. Cell Biol.* **2006**, *8*, 1163–1170. [[CrossRef](#)]
30. Snapp, E.L.; Hegde, R.S.; Francolini, M.; Lombardo, F.; Colombo, S.; Pedrazzini, E.; Borgese, N.; Lippincott-Schwartz, J. Formation of stacked ER cisternae by low affinity protein interactions. *J. Cell Biol.* **2003**, *163*, 257–269. [[CrossRef](#)]
31. Lu, M.; Banetta, L.; Young, L.J.; Smith, E.J.; Bates, G.P.; Zaccane, A.; Kaminski Schierle, G.S.; Tunnacliffe, A.; Kaminski, C.F. Live-cell super-resolution microscopy reveals a primary role for diffusion in polyglutamine-driven aggresome assembly. *J. Biol. Chem.* **2019**, *294*, 257–268. [[CrossRef](#)] [[PubMed](#)]
32. Laine, R.F.; Sinnige, T.; Ma, K.Y.; Haack, A.J.; Poudel, C.; Gaida, P.; Curry, N.; Perni, M.; Nollen, E.A.A.; Dobson, C.M.; et al. Fast Fluorescence Lifetime Imaging Reveals the Aggregation Processes of alpha-Synuclein and Polyglutamine in Aging *Caenorhabditis elegans*. *ACS Chem. Biol.* **2019**, *14*, 1628–1636. [[CrossRef](#)] [[PubMed](#)]
33. Ossato, G.; Digman, M.A.; Aiken, C.; Lukacsovich, T.; Marsh, J.L.; Gratton, E. A two-step path to inclusion formation of huntingtin peptides revealed by number and brightness analysis. *Biophys. J.* **2010**, *98*, 3078–3085. [[CrossRef](#)] [[PubMed](#)]
34. Li, L.; Liu, H.; Dong, P.; Li, D.; Legant, W.R.; Grimm, J.B.; Lavis, L.D.; Betzig, E.; Tjian, R.; Liu, Z. Real-time imaging of Huntingtin aggregates diverting target search and gene transcription. *eLife* **2016**, *5*, e17056. [[CrossRef](#)]
35. Sahl, S.J.; Lau, L.; Vonk, W.I.; Weiss, L.E.; Frydman, J.; Moerner, W.E. Delayed emergence of subdiffraction-sized mutant huntingtin fibrils following inclusion body formation. *Q. Rev. Biophys.* **2016**, *49*, e2. [[CrossRef](#)]
36. Sahl, S.J.; Weiss, L.E.; Duim, W.C.; Frydman, J.; Moerner, W.E. Cellular inclusion bodies of mutant huntingtin exon 1 obscure small fibrillar aggregate species. *Sci. Rep.* **2012**, *2*, 895. [[CrossRef](#)]
37. Bhardwaj, V.; Panicker, M.M.; Udgaonkar, J.B. Fluorescence anisotropy uncovers changes in protein packing with inclusion growth in a cellular model of polyglutamine aggregation. *Biochemistry* **2014**, *53*, 3621–3636. [[CrossRef](#)]
38. Caron, N.S.; Hung, C.L.; Atwal, R.S.; Truant, R. Live cell imaging and biophotonic methods reveal two types of mutant huntingtin inclusions. *Hum. Mol. Genet.* **2014**, *23*, 2324–2338. [[CrossRef](#)]

39. Hansen, C.V.; Schroll, H.J.; Wüstner, D. A discontinuous Galerkin model for fluorescence loss in photobleaching of intracellular polyglutamine protein aggregates. *BMC Biophys.* **2018**, *11*, 7. [[CrossRef](#)]
40. Hansen, C.V.; Schroll, H.J.; Wustner, D. A Discontinuous Galerkin Model for Fluorescence Loss in Photobleaching. *Sci. Rep.* **2018**, *8*, 1387. [[CrossRef](#)]
41. Schmid, P.J. Dynamic mode decomposition of numerical and experimental data. *J. Fluid Mech.* **2010**, *656*, 5–28. [[CrossRef](#)]
42. Brunton, S.L.; Kutz, J.N. *Data-Driven Science and Engineering: Machine Learning, Dynamical Systems, and Control*; Cambridge University Press: Cambridge, UK, 2019.
43. Bi, C.; Yuan, Y.; Zhang, J.W.; Shi, Y.; Xiang, Y.; Wang, Y.; Zhang, R.H. Dynamic Mode Decomposition Based Video Shot Detection. *IEEE Access* **2018**, *6*, 21397–21407. [[CrossRef](#)]
44. Kutz, J.N.; Fu, X.; Brunton, S.L.; Erichson, N.B. Multi-resolution dynamic mode decomposition for foreground/background separation and object tracking. In Proceedings of the 2015 IEEE International Conference on Computer Vision Workshop, Santiago, Chile, 7–13 December 2015.
45. Tirunagari, S.; Poh, N.; Wells, K.; Bober, M.; Gorden, I.; Windridge, D. Functional Segmentation through Dynamic Mode Decomposition: Automatic Quantification of Kidney Function in DCE-MRI Images. *arXiv* **2019**, arXiv:1905.10218.
46. Casorso, J.; Kong, X.; Chi, W.; Van De Ville, D.; Yeo, B.T.T.; Liegeois, R. Dynamic mode decomposition of resting-state and task fMRI. *Neuroimage* **2019**, *194*, 42–54. [[CrossRef](#)]
47. Wüstner, D. Image segmentation and separation of spectrally similar dyes in fluorescence microscopy by dynamic mode decomposition of photobleaching kinetics. *BioRxiv* **2022**, bioRxiv:2022.02.28.482234.
48. Erichson, N.B.J.; Brunton, S.L.; Kutz, N. Compressed dynamic mode decomposition for background modeling. *J. Real-Time Image Process.* **2019**, *16*, 1479–1492. [[CrossRef](#)]
49. Gavish, M.; Donoho, D.L. The optimal hard threshold for singular values is $4/\sqrt{3}$. *IEEE Trans. Inf. Theory* **2014**, *60*, 5040–5063. [[CrossRef](#)]
50. Demo, N.; Tezzele, M.; Rozza, G. PyDMD: Python Dynamic Mode Decomposition. *J. Open Source Softw.* **2018**, *3*, 530. [[CrossRef](#)]
51. Brandt, S. *Datenanalyse*; Springer: Berlin/Heidelberg, Germany, 1999.
52. Barlett, V.R.; Hoyuelos, M.; Martin, H.O. Comparison between fixed and Gaussian steplength in Monte Carlo simulations for diffusion processes. *J. Comput. Phys.* **2011**, *230*, 3719–3726. [[CrossRef](#)]
53. Istratov, A.A.; Vyvenko, O.F. Exponential analysis in physical phenomena. *Rev. Sci. Instrum.* **1999**, *70*, 1233–1257. [[CrossRef](#)]
54. Tschumperle, D.; Deriche, R. Vector-valued image regularization with PDE's: A common framework for different applications. *IEEE Trans. Pattern Anal. Mach. Intell.* **2005**, *27*, 506–517. [[CrossRef](#)] [[PubMed](#)]
55. Delpretti, S.; Luisier, F.; Ramani, S.; Blu, T.; Unser, M. Multiframe SURE-LET denoising of timelapse fluorescence microscopy images. In Proceedings of the 5th IEEE International Symposium on Biomedical Imaging: From Nano to Macro, Paris, France, 14–17 May 2008; pp. 149–152.
56. Viguierie, A.; Barros, G.F.; Grave, M.; Reali, A.; Coutinho, A.L. Coupled and uncoupled dynamic mode decomposition in multi-compartmental systems with applications to epidemiological and additive manufacturing problems. *Comput. Methods Appl. Mech. Eng.* **2022**, *391*, 114600. [[CrossRef](#)]
57. Le Clainche, S.; Vega, J.M. Higher order dynamic mode decomposition. *SIAM J. Appl. Dyn. Sys.* **2017**, *16*, 882–925. [[CrossRef](#)]
58. Baddoo, P.J.; Herrmann, B.; McKeon, B.J.; Kutz, J.N.; Brunton, S.L. Physics-informed dynamic mode decomposition (piDMD). *arXiv* **2021**, arXiv:2112.04307.
59. Williams, M.O.; Kevrekidis, I.G.; Rowley, C.W. A Data-Driven Approximation of the Koopman Operator: Extending Dynamic Mode Decomposition. *J. Nonlinear Sci.* **2015**, *25*, 1307–1346. [[CrossRef](#)]
60. Rudy, S.H.; Brunton, S.L.; Proctor, J.L.; Kutz, J.N. Data-driven discovery of partial differential equations. *Sci. Adv.* **2017**, *3*, e1602614. [[CrossRef](#)]
61. Wüstner, D.; Christensen, T.; Solanko, L.M.; Sage, D. Photobleaching kinetics and time-integrated emission of fluorescent probes in cellular membranes. *Molecules* **2014**, *19*, 11096–11130. [[CrossRef](#)]
62. Cardarelli, F.; Tosti, L.; Serresi, M.; Beltram, F.; Bizzarri, R. Fluorescent recovery after photobleaching (FRAP) analysis of nuclear export rates identifies intrinsic features of nucleocytoplasmic transport. *J. Biol. Chem.* **2012**, *287*, 5554–5561. [[CrossRef](#)]
63. Wüstner, D. Mathematical analysis of hepatic high density lipoprotein transport based on quantitative imaging data. *J. Biol. Chem.* **2005**, *280*, 6766–6779. [[CrossRef](#)]